CRYSTAL GROWTH & DESIGN

Article

Cite This: Cryst. Growth Des. 2018, 18, 4306−4319

pubs.acs.org/crystal

Polymorph Selection by Continuous Precipitation

Thomas C. Farmer,[†] Sina K. Schiebel,[†,‡] Bradley F. Chmelka,[†] and Michael F. Doherty*[,†]

[†]Department of Chemical Engineering, University of California, Santa Barbara, California 93106, United States

Supporting Information

ABSTRACT: When the dominant rate-mechanisms within a mixed-suspension mixed-product removal (MSMPR) crystallizer are secondary nucleation and size-independent linear crystal growth, the effluent crystal distribution is guaranteed to exhibit a single polymorphic solid form at steady state. However, multiple solid forms are often simultaneously observed during the continuous precipitation of $CaCO_3$. Accounting for agglomeration within the population balance reconciles model predictions with experiments. Here, we elucidate the steady state structure and linear stability features of an agglomeration-enabled continuous precipitator model. We demonstrate that one can make rational process design and operation decisions to select the effluent solid form, regardless of its thermodynamic stability. Specifically, we utilize these results to choose process conditions that yield pure, thermodynamically metastable vaterite during $CaCO_3$ precipitation, based on powder X-ray diffraction, solid-state ^{43}Ca NMR, and scanning electron microscopy. This new design framework enables predictive modeling of $CaCO_3$ precipitation, but more generally, it is expected to enable rational decision making during the design and operation of other agglomerative precipitation processes for which solid form selection is desired.

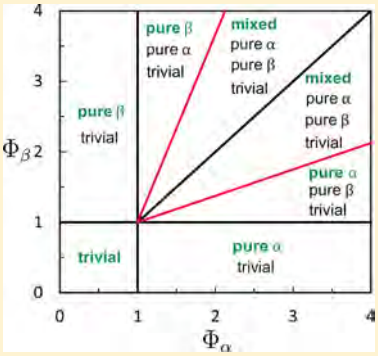

INTRODUCTION

Polymorphism has been prominent in the study of material science and industrial crystallization for over 180 years,[1,2] and the primary mechanism of polymorphic interconversion, known as solvent-mediated phase transformation, has been postulated, modeled, and experimentally validated over the past 35 years.[3−5] Polymorph selection and control has maintained attention over such long periods of time due to the technological implications of polymorphic variation of a compound's mechanical, electrical, optical, chemical, solubility, bioavailabillity, and bioactivity properties.[6−9] Controlling polymorphism in industrial processes has remained difficult and at times elusive, as demonstrated by the extensive literature on concentration control, temperature control, additive selection, templating materials, solvent choice, and combinatoric screening.[10−18] Recently, the ability to produce single polymorph crystal distributions using continuous crystallization has been demonstrated for L-glutamic acid and *p*-aminobenzoic acid systems.[19,20] At steady state, a MSMPR crystallizer operates at a single solute concentration and supersaturation. Thus, each solid form is either supersatured or undersaturated. If a form is undersaturated, it will eventually wash out of the crystallizer and be absent at steady state. Therefore, the solvent mediated phase transformation cannot occur at steady state in a continuous MSMPR crystallizer. These observations motivated the development of general design rules for producing pure distributions of any preferred polymorph in a continuous crystallizer dominated by size-independent linear crystal growth and secondary nucleation, regardless of the thermodynamic stability of the desired solid form.[21] This is an unrestrictive set of assumptions that covers many organic crystal systems, including the vast majority of pharmacologically active small molecules.[22,23]

Still, there are other crystal/crystallizer systems of industrial relevance for which other rate-processes could become important. For example, a process could exhibit (1) primary nucleation, (2) metastable-form nucleation from the surface of a relatively stable form, (3) alternative growth or nucleation rate expressions, (4) agglomeration, (5) breakage, (6) chemical reaction in solution, or (7) a number of possible process permutations (e.g., putting two devices in series, recycling solids, etc.). The first three of these were discussed and classified as qualitatively unimportant for purposes of solid form selection during well-mixed, continuous crystallizations in our previous publication.[21] The last four have not yet been considered and are expected to become important in some crystal systems.

One system of special interest is the reactive precipitation of $CaCO_3$ from Na_2CO_3 and $CaCl_2$. This system exhibits chemical reaction in solution, significant agglomeration, and five unique solid forms near standard temperature and pressure (STP): 3 crystalline polymorphs, a crystalline hydrate, and an amorphous form.[24] Furthermore, it is technologically interesting because of efforts to make cementitious materials from flue gases for carbon capture. For this type of process to work, the solids produced must exhibit suitable material properties for structural materials applications. The patent literature suggests that the thermodynamically stable form of $CaCO_3$ (calcite) is unlikley to make a suitable construction material, while vaterite

Received: January 19, 2018
Revised: June 11, 2018
Published: June 12, 2018

Downloaded via UNIV OF CALIFORNIA SANTA BARBARA on August 3, 2018 at 17:06:19 (UTC).
See https://pubs.acs.org/sharingguidelines for options on how to legitimately share published articles.

© 2018 American Chemical Society

DOI: 10.1021/acs.cgd.8b00116
Cryst. Growth Des. 2018, 18, 4306−4319

(highest energy crystalline form) and amorphous calcium carbonate (ACC, highest energy amorphous form) seem to work quite well.[25,26] Therefore, we are presented with the specific challenge of directing solid form during $CaCO_3$ precipitation as a step toward developing carbon capture and utilization processes.

Still, there are many other systems for which solid form selection is a pivotal engineering objective, so here, we address the general challenge of polymorph selection during agglomerative precipitations. Agglomeration events decrease total crystal number density and reduce total crystal surface area. Crystals grow from the surface, so less crystal surface area implies a lower *total* (distribution integrated) growth rate. Therefore, agglomeration changes the relative magnitudes of growth, nucleation, and product removal rates within a crystallizer. Altering the relative rates has a significant effect on the dynamic stability of the various steady states and therefore on the design rules for solid form selection.

We have characterized the impact of agglomeration on the steady state multiplicity and relative steady state dynamic stability by generating and analyzing a bipolymorph agglomeration-enabled precipitator model. We have demonstrated that adding agglomeration to the model enables the mixed-polymorph steady states that are often observed during the continuous precipitation of $CaCO_3$, but were unpredictable with a nonagglomerating, continuous crystallizer model.[21] The insights gained from analyzing the agglomeration-enabled model can be used to direct polymorphism in agglomerative systems such as the technologically, geologically, and biologically important $CaCO_3$ system.

Experimental measurements confirmed the model predictions, yielding pure metastable polymorphs under steady state process conditions. Polymorph selection can be achieved through manipulation of the dynamic stability of competing steady states in a continuous device through this type of process design. Under such circumstances, the resulting process is inherently simple to control, and process disturbances tend to decay with time. Furthermore, the thermodynamically metastable vaterite crystals generated in this way do not transform to the more stable calcite polymorph over the time scales we have thus far measured and observed (>12 months).

THEORY: MODEL EQUATIONS

The semantic distinction between precipitation and crystallization has different meanings to different investigators.[27,28] Here, we use the term precipitation to encompass the class of crystallization processes characterized by very high solute supersaturations. These supersaturations are typically generated by chemical reaction of two soluble reactants to form a sparingly soluble product. In these processes, desupersaturation is typically dominated by nucleation, and large crystals form primarily from the agglomeration of many smaller crystals. Crystallization is characterized by lower supersaturations, in which the desupersaturation is dominated by crystal growth. In crystallization, agglomeration tends to have less of an impact on the final distribution of crystal sizes. Often, all three mechanisms need to be taken into account (e.g., $CaCO_3$ precipitation at high supersaturation and paracetamol crystallization at lower supersaturations[29]), and naming the method of crystal formation becomes more a matter of preference and tradition. Some precipitative systems can be described as if the crystal growth rates are exactly zero,[30] but this is not a reasonable approximation for crystallizations.

A multipolymorph continuous precipitation process can be modeled as the system of partial differential integral equations shown in eqs 1−6. These equations are generated by applying a population balance and a solute/mass balance to a multipolymorph, continuous, mixed-suspension, mixed-product-removal (MSMPR) crystallizer. A population balance model is a mathematical expression of conservation of a distributed quantity under the influence of some rate mechanisms described by constitutive rate laws. Therefore, a population balance describes how a distribution changes as a function of time. In this case, that distibution is the crystal size distribution, $n_i(t, x)$, where $n_i(t, x)$ denotes the crystal number density of form i as a function of t (time) and x (crystal length, if spherical then x is crystal radius or diameter). This distribution has units of number per volume per length, such that the integral $\int_{x_a}^{x_b} n_i(t, x)\,\mathrm{d}x$ gives the crystal number density of solid form i between the lengths x_a and x_b as a function of t. For an agglomeration-enabled continuous precipitator, the relevant rate processes that require a constitutive rate law are secondary nucleation (B_i), size-independent linear crystal growth (G_i), and crystal agglomeration. The rate expressions we have chosen for nucleation and growth are given in eq 2. These expressions simplify to eq 6 when the feed is stoichiometric (see the SI for discussion of the nonstoichiometric feed case). We discussed these rate expression choices in detail in our previous paper and demonstrated that the analysis and results are qualitatively similar for different sets of rate expressions.[21] In fact, the only significant change in the governing system of equations from our previous paper is the notable addition of the two integral terms that describe crystal agglomeration. The first integral term quantifies the combined crystal number density available to form a crystal of length x, as a function of x. The second integral term quantifies the combined crystal number density available for removal from the distribution due to agglomeration events involving a crystal of size x, as a function of x. In both cases, the combined crystal number density is converted to an agglomeration rate through an agglomeration kernel β_i (agglomeration frequency rate coefficient). In general, β_i can be a function of size (x) and supersaturation (S, the ratio of the solute concentration in the device to its saturation concentration), but it will be considered a constant throughout this article. A size and supersaturation independent kernel and the integral expressions in eq 1 combine to give the simplest possible description of agglomeration that conserves volume/mass when the crystal size coordinate has units of length.[31,32] The agglomeration kernel used here also implies that agglomeration events can only occur among particles in the same distribution (of the same solid form). Additional discussion and justification of the selected agglomeration kernel is included in the SI. The initial and boundary conditions are standard and discussed elsewhere.[31,33] The resulting partial differential integral equation that governs the distribution dynamics of form i is shown in eqs 1−3.

$$\frac{\partial n_i}{\partial t} + G_i\frac{\partial n_i}{\partial x} = -\frac{n_i}{\tau} + \frac{\beta_i x^2}{2}\int_0^x \frac{n_i((x^3-\lambda^3)^{1/3})n_i(\lambda)}{(x^3-\lambda^3)^{2/3}}\,\mathrm{d}\lambda - \beta_i n_i(x)\int_0^\infty n_i(\lambda)\,\mathrm{d}\lambda \quad (1)$$

DOI: 10.1021/acs.cgd.8b00116
Cryst. Growth Des. 2018, 18, 4306−4319

$$B_i = k_{i,b}\left[\left(\frac{C_1C_2}{K_{\mathrm{eq},i}}\right)^{1/2} - 1\right]^{b_i} \int_0^\infty x^2 n_i(t, x)\,\mathrm{d}x$$
$$G_i = k_{i,g}\left[\left(\frac{C_1C_2}{K_{\mathrm{eq},i}}\right)^{1/2} - 1\right]^{g_i} \tag{2}$$

$$i = \alpha, \beta \qquad n_i(t = 0, x) = n_{i,\mathrm{seed}} \qquad n_i(t, x = 0) = \frac{B_i}{G_i} \tag{3}$$

where $n_{i,\mathrm{seed}}$ is a distribution of seed crystals introduced as a pulse at $t = 0$, $K_{\mathrm{eq},i}$ is the equilibrium solubility constant for form i, C_1 and C_2 are the molar concentrations of Ca^{2+} and CO_3^{2-} ions in solution, respectively, and τ is the MSMPR residence time. The 1/2 power that appears in the growth and nucleation driving forces was justified in a previous publication.[34] In general, there are p polymorphs, denoted by the subscript i. Here, the two-solid-form case is explicitly considered and analyzed, with the thermodynamically stable form at STP (calcite) labeled $i = \beta$ and the thermodynamically metastable form (vaterite) labeled $i = \alpha$ (consistent with our previous work).[21]

Another modification to the previous model arises due to the reaction chemistry inherent in this type of reactive precipitation process. The chemistry adds additional mole balance ODEs and additional model parameters and design choices related to the reaction rates and the feed stoichiometry. When the feed is stoichiometric and the pH is relatively high, the mole balance ODEs and the growth and nucleation rate expressions simplify to eqs 4 and 6, as discussed in detail in the Supporting Information. These conditions will be met for the experiments discussed throughout this article.

$$\frac{\mathrm{d}C}{\mathrm{d}t} = \frac{C_0 - C}{\tau} - \sum_{i=\alpha,\beta} \rho_i k_{i,v} k_{i,g}\left(\frac{C}{K_{\mathrm{eq},i}^{1/2}} - 1\right)^{g_i} \int_0^\infty n_i x^2\,\mathrm{d}x \tag{4}$$

$$C(t = 0) = C_0 \tag{5}$$

$$B_i = k_{i,b}\left(\frac{C}{K_{\mathrm{eq},i}^{1/2}} - 1\right)^{b_i} \int_0^\infty x^2 n_i(t, x)\,\mathrm{d}x$$
$$G_i = k_{i,g}\left(\frac{C}{K_{\mathrm{eq},i}^{1/2}} - 1\right)^{g_i} \tag{6}$$

where ρ_i is the molar density of solid form i and $k_{i,v}$ is a shape factor. A derivation of these equations and a discussion of the implication of a nonstoichiometric feed are both available in the Supporting Information. It is also worth noting that all of the concentrations, equilibrium constants, and densities have been defined on a molar basis here. A mass basis was used in the previous, nonagglomerating model, but a mole basis is more convenient when chemical reactions occur.

Fixed Point Quadrature Method of Moments (F-QMOM). The method of moments is an integral transformation that allows one to monitor and analyze the moments of a distribution, instead of considering the entire distribution. This transformation finds utility in applications for which a more detailed knowledge of a distribution's dynamics is unnecessary. Here, we are concerned with determining process conditions for which a crystal size distribution under the influence of nucleation, growth, agglomeration, and convective flow exhibits one solid form or another. This problem is an ideal candidate for the method of moments because the relative fraction of each form can be determined from the moments of each distribution alone. Typically, application of the method of moments is restricted to cases in which the moment ODEs close. Closure occurs when the dynamics of some set of moments can be described in terms of only model parameters and moments of order $k \leq N$ (where k is the subscript denoting the moment order, and N is the total number of moments necessary for closure). Closure is not met when the moment transformation fails to remove all of the $n_i(t,x)$ terms or when lower-order moments always depend on higher-order moments, necessitating a solution of the full PDE or of the entire infinite set of moment equations, respectively. Applying the method of moments and a change of variables ($u^3 = x^3 - \lambda^3$)[35] to the agglomeration (integral) terms in eq 1 results in eq 7 for the kth moment of the i distribution

$$\int_0^\infty x^k\left[\frac{\beta_i x^2}{2}\int_0^x \frac{n_i((x^3 - \lambda^3)^{1/3}) n_i(\lambda)}{(x^3 - \lambda^3)^{2/3}}\,\mathrm{d}\lambda - \beta_i n_i(x)\int_0^\infty n_i(\lambda)\,\mathrm{d}\lambda\right]\mathrm{d}x$$
$$= \frac{\beta_i}{2}\int_0^\infty n_i(\lambda)\int_0^\infty (u^3 + \lambda^3)^{k/3} n_i(u)\,\mathrm{d}u\,\mathrm{d}\lambda - \beta_i m_{i,k} m_{i,0} \tag{7}$$

where $m_{i,k}$ is the kth moment of the i distribution (the method of moments is described in more detail in the Supporting Information). Unfortunately, the transformation does not close as defined, though closure can be enforced numerically with a technique termed the quadrature method of moments (QMOM).[36] The QMOM utilizes only the moments of a distribution to estimate integrals over the unknown distribution. The quadrature rule can be defined from the moments using the product-difference algorithm developed by Gordon,[37] by reformulating the model as a system of differential algebraic equations (DAE) using the algebraic definition of the quadrature rule,[38] by tracking the weights and abscissas of the quadrature rule directly through a Jacobian matrix transformation,[39] or by fixing the abscissas at zeros of an orthogonal basis set and directly calculating the weights such that the known moments are recreated exactly.[40] The latter method has been named the fixed point quadrature method of moments (F-QMOM) and is used here. With the moments defined from the moment ODEs and the abscissas (L_j) defined as zeros of some orthogonal basis set, the weights (μ_j) can be calculated from eq 8

$$m_k = \sum_j L_j^k \mu_j \tag{8}$$

This can be written in matrix form by defining the matrix $\mathbf{Q}$

$$\mathbf{Q}_{l,j} = L_j^{l-1} \tag{9}$$

giving

$$\mathbf{m} = \mathbf{Q}\boldsymbol{\mu} \tag{10}$$

The abscissas or lengths in the quadrature rule can be chosen as the zeros of any orthgonal basis set of polynomials,

DOI: 10.1021/acs.cgd.8b00116
Cryst. Growth Des. 2018, 18, 4306−4319

although the choice of basis set will affect the computation speed and accuracy.[41] Once an orthogonal basis set is chosen, the abscissas are known, and the matrix **Q** becomes constant and known. Therefore, one can always define the weights as a known linear combination of the moments as in eq 11

$$\boldsymbol{\mu} = \mathbf{Q}^{-1}\mathbf{m} \tag{11}$$

Once the abscissas and weights are known, the remaining integral term in eq 7 can be rewritten as the sum in eq 12

$$\frac{\beta}{2}\int_0^\infty n(\lambda)\int_0^\infty (u^3+\lambda^3)^{k/3} n(u)\,du\,d\lambda = \frac{\beta}{2}\sum_l \mu_l \sum_j (L_l^3 + L_j^3)^{k/3}\mu_j \tag{12}$$

This can be rewritten again as a compact function of only the abscissas and moments by first defining a new three-dimensional matrix $\mathbf{F}_k$

$$\mathbf{F}_k(l,j) = \frac{1}{2}(L_l^3 + L_j^3)^{k/3} \tag{13}$$

then eq 12 becomes

$$\frac{\beta}{2}\int_0^\infty n(\lambda)\int_0^\infty (u^3+\lambda^3)^{k/3} n(u)\,du\,d\lambda = \beta \mathbf{m}'\mathbf{Q}^{-1'}\mathbf{F}_k\mathbf{Q}^{-1}\mathbf{m} \tag{14}$$

where $'$ represents a vector or matrix transpose. For every k, this vector-matrix multiplication results in a scalar sum of moment terms up to order $(N-1)$, where N is the number of moments tracked by the model. When written this way, one can increase the accuracy (and computation time) at will by increasing N and adding abscissas from higher-order polynomials in the same orthogonal basis set. (Care should also be taken to scale the moments, such that the distribution can be accurately represented by abscissas $\in[0, 1]$). After nondimensionalization (details in Supporting Information), the resulting model contains $3p + 1$ ODEs and $5p - 1$ parameters, where p is the number of solid forms included in the model. When considering a metastable polymorph (e.g., vaterite = α) and a stable polymorph (e.g., calcite = β), $p = 2$, and there are $5p-1 = 9$ dimensionless parameters of which $2p$ are exponents in the growth and nucleation rate laws (g_i and b_i). The others are combinations of physical parameters that make up dimensionless groups. For example, $p - 1$ of these dimensionless groups are solubility factors that quantify the differences in nucleation and growth driving forces among the various solid forms (γ)

$$\gamma = \frac{K_{\mathrm{eq},\beta}^{1/2} - K_{\mathrm{eq},\alpha}^{1/2}}{C_0 - K_{\mathrm{eq},\beta}^{1/2}} < 0 \tag{15}$$

The other $2p$ are relative rates that can be rationally manipulated (or engineered) by the intelligent selection of process variables such as temperature, inlet supersaturation, residence time, and solvent. These are termed Damköhler (Da_i) and Agglomeration (A_i) numbers

$$\mathrm{Da}_\alpha = 2\tau k_{\alpha,b}\left(\frac{C_0 - K_{\mathrm{eq},\beta}^{1/2}}{K_{\mathrm{eq},\alpha}^{1/2}}\right)^{b_\alpha}\sigma_\alpha^2 > 0$$

$$\mathrm{Da}_\beta = 2\tau k_{\beta,b}\left(\frac{C_0 - K_{\mathrm{eq},\beta}^{1/2}}{K_{\mathrm{eq},\beta}^{1/2}}\right)^{b_\beta}\sigma_\beta^2 > 0 \tag{16}$$

$$A_\alpha = \frac{\beta_\alpha \tau}{8\pi\sigma_\alpha^3}\frac{(C_0 - K_{\mathrm{eq},\alpha}^{1/2})}{\rho_\alpha} > 0$$

$$A_\beta = \frac{\beta_\beta \tau}{8\pi\sigma_\beta^3}\frac{(C_0 - K_{\mathrm{eq},\beta}^{1/2})}{\rho_\beta} > 0 \tag{17}$$

where σ_i is the characteristic growth length for form i defined as

$$\sigma_\alpha = \tau k_{\alpha,g}\left(\frac{C_0 - K_{\mathrm{eq},\beta}^{1/2}}{K_{\mathrm{eq},\alpha}^{1/2}}\right)^{g_\alpha} \qquad \sigma_\beta = \tau k_{\beta,g}\left(\frac{C_0 - K_{\mathrm{eq},\beta}^{1/2}}{K_{\mathrm{eq},\beta}^{1/2}}\right)^{g_\beta} \tag{18}$$

All variables are defined in the notation section, and the nondimensionalization procedure that leads to these dimensionless groups is detailed in the Supporting Information.

The Damköhler numbers are given this name due to their physicochemical similarity to the Damköhler numbers in reaction engineering. These groups are ratios of the residence time to the crystallization time of each form, such that the rates of nucleation and growth of form i are fast relative to the process residence time when Da_i is large, and slow when Da_i is small. The Da_α group depends both on $K_{\mathrm{eq},\beta}^{1/2}$ and $K_{\mathrm{eq},\alpha}^{1/2}$ because the solute concentration is nondimensionalized with respect to $K_{\mathrm{eq},\beta}^{1/2}$ (see the Supporting Information for additional discussion). The Damköhler numbers and the solubility correction factor (γ) were discussed in detail in our earlier paper, although the notation is slightly different here due to the reaction chemistry (to translate from one to the other, set $C_{\mathrm{sat},i} = K_{\mathrm{eq},i}^{1/2}$). The Agglomeration numbers are a new feature of the agglomeration-enabled population balance model. Each Agglomeration number is a ratio of the process time (τ) to the agglomeration time associated with that form ($\approx\beta_i^{-1}$). Therefore, agglomeration becomes a more dominant rate process within the precipitator as the Agglomeration numbers increase.

Now, the ODE system can be presented in terms of the vector/matrix operations referenced in eq 14, the dimensionless moments ($\omega_{i,k} \in [0, \infty)$), the dimensionless time ($\xi \in [0, \infty)$), the dimensionless solute concentration ($y \in [0, 1]$), and the dimensionless groups. The $3p + 1 = 7$ resulting ODEs are

$$\frac{d\omega_{\alpha,0}}{d\xi} = -\omega_{\alpha,0} + \mathrm{Da}_\alpha(y+\gamma)^{b_\alpha}\omega_{\alpha,2} - \frac{A_\alpha}{2}\omega_{\alpha,0}^2 \tag{19}$$

$$\frac{d\omega_{\alpha,1}}{d\xi} = -\omega_{\alpha,1} + (y+\gamma)^{g_\alpha}\omega_{\alpha,0} + A_\alpha(\boldsymbol{\omega}_\alpha'\mathbf{Q}^{-1'}\mathbf{F}_1\mathbf{Q}^{-1}\boldsymbol{\omega}_\alpha - \omega_{\alpha,1}\omega_{\alpha,0}) \tag{20}$$

$$\frac{d\omega_{\alpha,2}}{d\xi} = -\omega_{\alpha,2} + (y+\gamma)^{g_\alpha}\omega_{\alpha,1} + A_\alpha(\boldsymbol{\omega}_\alpha'\mathbf{Q}^{-1'}\mathbf{F}_2\mathbf{Q}^{-1}\boldsymbol{\omega}_\alpha - \omega_{\alpha,2}\omega_{\alpha,0}) \tag{21}$$

DOI: 10.1021/acs.cgd.8b00116
Cryst. Growth Des. 2018, 18, 4306−4319

$$\frac{d\omega_{\beta,0}}{d\xi} = -\omega_{\beta,0} + Da_\beta y^{b_\beta}\omega_{\beta,2} - \frac{A_\beta}{2}\omega_{\beta,0}^2 \quad (22)$$

$$\frac{d\omega_{\beta,1}}{d\xi} = -\omega_{\beta,1} + y^{g_\beta}\omega_{\beta,0} + A_\beta(\boldsymbol{\omega}_\beta{}'\mathbf{Q}^{-1'}\mathbf{F}_1\mathbf{Q}^{-1}\boldsymbol{\omega}_\beta - \omega_{\beta,1}\omega_{\beta,0}) \quad (23)$$

$$\frac{d\omega_{\beta,2}}{d\xi} = -\omega_{\beta,2} + y^{g_\beta}\omega_{\beta,1} + A_\beta(\boldsymbol{\omega}_\beta{}'\mathbf{Q}^{-1'}\mathbf{F}_2\mathbf{Q}^{-1}\boldsymbol{\omega}_\beta - \omega_{\beta,2}\omega_{\beta,0}) \quad (24)$$

$$\frac{dy}{d\xi} = 1 - y - \omega_{\beta,2}y^{g_\beta} - \omega_{\alpha,2}(y+\gamma)^{g_\alpha} \quad (25)$$

In the limit A_α, $A_\beta \to 0$, the original, nonagglomerating model is recovered.[21] More details on the derivation and nondimensionalization of both the stoichiometric (presented here) and nonstoichiometric feed cases are provided in the Supporting Information.

Parameter Continuation of Model Elucidates Steady State Structure. Ideally, process engineers seek to understand how process outputs change as functions of design and operation decision variables. Some systems exhibit steady state multiplicity, and in these systems, process dynamics play a significant role in process design. Relating decision variables to process outputs requires relating decision variables to the relative dynamic stability of the qualitatively distinct steady states. With this information, one can make rational design decisions such that a preferred steady state is obtained and maintains its dynamic stability. When this procedure proves difficult or impossible, one can typically design new degrees of freedom to expand the range of attainable outcomes (for polymorph selection, one could imagine adding a solids recycle, multiple crystallizers in series, templating additives in the feed, changing the solvent, etc.).

This precipitator model predicts 4 qualitatively distinct steady states: (1) trivial, (2) pure α polymorph, (3) pure β polymorph, and (4) a mixed-polymorph steady state. The trivial steady state occurs for processes exhibiting relatively low Damköhler numbers, when the MSMPR residence time is small relative to the characteristic nucleation and growth times of both forms. In this limit, it is possible for the supersaturated solution to flow into and out of the precipitator without any precipitation occurring. The pure polymorph steady states are characterized by one of the polymorphs being completely absent from the reactor/crystallizer. The mixed-polymorph steady state is characterized by nonzero amounts of both polymorphs coexisting in the reactor at steady state. The first three steady states were predicted by our previous nonagglomerating model,[21] but the last one is unique to the agglomerating precipitator model. In some regions of parameter space (i.e., for some sets of dimensionless parameters implied by some choice of T, C_0, and τ), only the trivial steady state is possible. In other regions, two, three, or four of the steady states described above become possible solutions to the set of steady state algebraic equations implied by the ODEs in eqs 19−25. For any set of parameters, only one of these steady states will be dynamically stable, and that is the one that the system will evolve toward and eventually stabilize at.

The relationship between the parameters and the steady state multiplicity is presented schematically in Figure 1. The

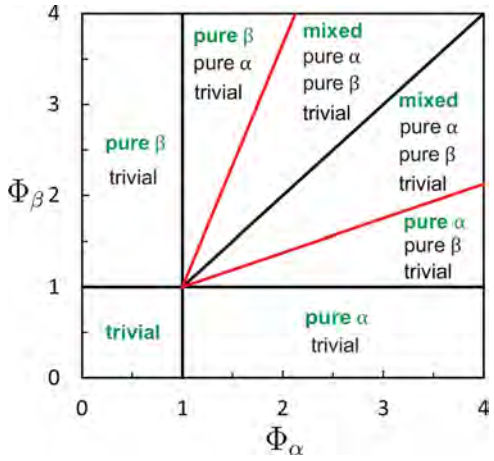

Figure 1. Steady state multiplicity diagram, in which Φ_β is plotted vs Φ_α with parameter regions labeled to indicate the steady states that are possible in the set of processes implied by each region of parameter space. The steady state that is dynamically stable in each region is labeled in green, bold face. The black lines represent projections of bifurcation surfaces that are not functions of the Agglomeration numbers. The red bifurcation surfaces collapse to the $\Phi_\alpha = \Phi_\beta$ line in the limit A_α, $A_\beta \to 0$. They collapse to the $\Phi_\alpha = 1$ and $\Phi_\beta = 1$ lines in the limit A_α, $A_\beta \to \infty$. They are shown here schematically for $A_\beta = A_\alpha \neq 0$. The stability parameters (Φ_i on the axes) are defined in eqs 26 and 27.

axes of Figure 1 contain two new dimensionless parameter combinations, Φ_α and Φ_β. In our earlier paper, a linear stability analysis of the nonagglomerating model demonstrated that these two combinations of parameters determine the relative dynamic stability of the available steady states. All of the bifurcations and steady state dynamic stability transitions in the nonagglomerating model take on simple functional forms when presented in terms of these stability groups, Φ_α and Φ_β. This construction allowed us to present all of the potential process design trade-offs, bifurcations, and stability transitions on a single two-dimensional figure, even though the model contained seven dimensionless parameters. The stability groups are defined in terms of the seven dimensionless model parameters from the nonagglomerating model in eqs 26 and 27

$$\Phi_\alpha = \left[Da_\alpha^{-1/(2g_\alpha+b_\alpha)} - \gamma\right]^{-1} \quad (26)$$

$$\Phi_\beta = \left[Da_\beta^{-1/(2g_\beta+b_\beta)}\right]^{-1} \quad (27)$$

Physically, Φ_i is the inverse of the dimensionless solute concentration (y) at the pure i polymorph steady state in the absence of agglomeration (i.e., y^{-1} when only form i is present and $A_i = 0$, see eqs 18 and 22 in our previous paper[21]). Therefore, Φ_i increases as the total solid deposition rate of form i increases. Qualitatively, one can think of these stability parameters as modified Damköhler numbers. Both stability groups are monotonically increasing functions of their respective Damköhler numbers, so it is qualitatively correct to equate the two when considering the results presented here.

DOI: 10.1021/acs.cgd.8b00116
Cryst. Growth Des. 2018, 18, 4306−4319

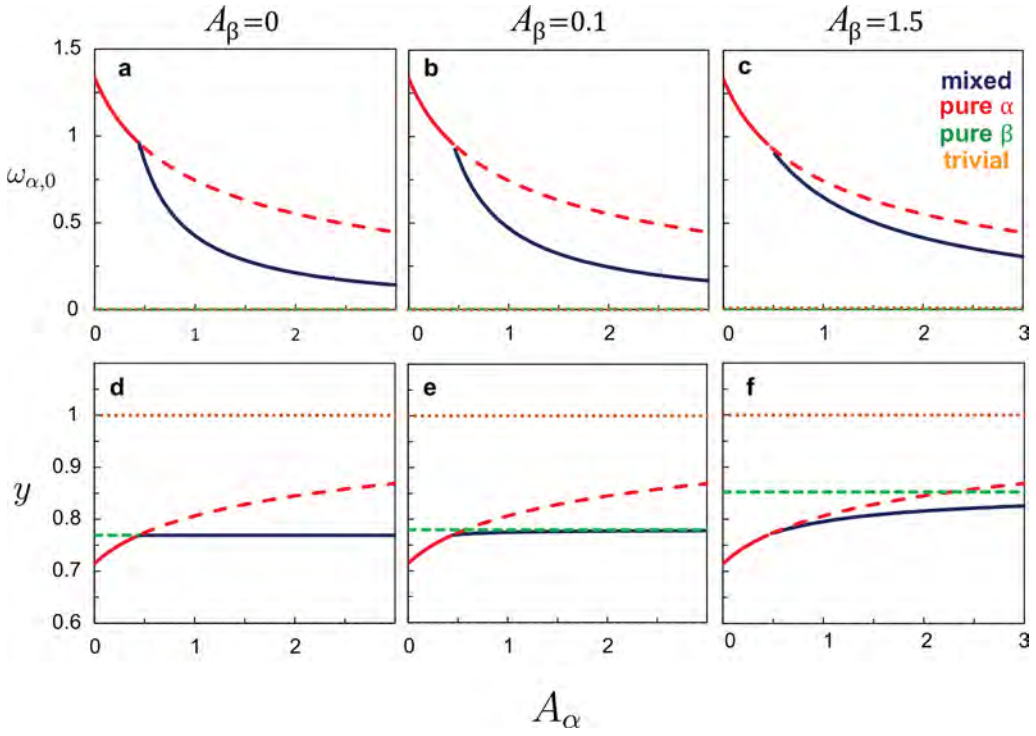

Figure 2. Bifurcation diagrams (state variables vs A_α) at fixed values of the stability groups (Φ_α = 1.4 and Φ_β = 1.3) for three values of the β form Agglomeration number, A_β; In (a) and (d), A_β = 0; (b) and (e), A_β = 0.1; (c) and (f), A_β = 1.5. $\omega_{\alpha,0}$ is the dimensionless steady state zeroth moment of the thermodynamically metastable polymorph distribution (dimensionless total α crystal number density). y is the dimensionless steady state solute concentration. Four qualitatively distinct steady states are present in the bifurcation diagrams. The mixed-polymorph steady state becomes possible when $A_\alpha \geq A_\alpha^{crit}$ (≈0.5 for this example). Per convention, dynamically stable steady states are represented as solid curves and unstable ones as dotted or dashed. These figures were generated with g_i = 1.5, b_i = 2.5, and γ = −0.0042, which are typical values representative of many systems for g_i and b_i. γ = −0.0042 is representative of the $CaCO_3$ experiments reported in this paper and is exact for the experiments described in Figure 5.

Quantitatively, the distinction remains important during process design.

The stability features of the agglomeration-enabled model are easiest to explain and interpret when presented in terms of the stability groups because several of the bifurcations and steady state dynamic stability transitions are independent of the Agglomeration numbers (discussed in detail later). Throughout this article, several figures will have these stability groups as axes because they represent a simple way to present the stability features of all of the potential processes one could build. When one makes a set of process choices (i.e., solvent, T, C_0, τ), a set of model parameters is implied (i.e., Da_i, g_i, b_i. γ, A_i). This set of parameters implies a value for the stability groups (Φ_α, Φ_β), which defines a point at some position on the stability or steady state multiplicity diagrams presented here. Therefore, each position on one of these diagrams represents a potential process, and one can intentionally move around the diagram by making rational design and operation decisions according to the various relationships among the model parameters and the stability groups described in eqs 15−18 and 26 and 27.

For example, Figure 1 shows how the steady state multiplicity changes as one varies the absolute and relative magnitudes of the stability groups (modified Damköhler numbers). Specifically, it indicates that the trivial steady state is the only possible steady state when the stability groups are both less than 1. As the stability groups increase, two, three, or four steady states become possible. The red lines separating the regions of three possible steady states from the regions of four possible steady states are the only curves on Figure 1 whose positions depend on the Agglomeration numbers. That dependence, and the relationship between the Φ_i, the A_i, and the dynamic stability of the different steady states will be discussed in detail in the next section.

The nonlinearities introduced by the agglomeration terms have prevented the determination of analytic expressions for the states as a function of the parameters at the various steady states. When a system of algebraic equations does not have an analytic solution such that the states can be written as explicit functions of the parameters, the parameter/solution structure can be elucidated through the use of a number of different numerical analysis techniques. Here, arc-length continuation was utilized to determine the steady state solution structure as a function of the parameters, Φ_α and Φ_β.[42−44] Figure 2 illustrates how the steady state structure varies as a function of A_α for a fixed value of Da_α, Da_β, γ, g_α, g_β, b_α and b_β and three select values of A_β (A_β = 0, 0.1, 1.5). The remaining parameters (Da_α, Da_β, γ g_α, g_β, b_α, and b_β) were chosen such that the metastable polymorph (α in general or vaterite specifically) is the only form present at steady state in the absence of agglomeration (i.e., Φ_α = 1.4, Φ_β = 1.3, A_α = A_β = 0). Along the ordinate in Figure 2a and d, both A_α and A_β are zero, corresponding to the nonagglomerating limit discussed in our previous paper.[21] At this point in parameter space, there are three distinct steady states. At the (dynamically unstable) trivial steady state, y = 1 and $\omega_{\alpha,0}$ = 0. By comparison, at the (dynamically stable) pure α steady state, y ≈ 0.72 and $\omega_{\alpha,0}$ ≈ 1.3. At the (dynamically unstable) pure β steady state, y ≈ 0.78

DOI: 10.1021/acs.cgd.8b00116
Cryst. Growth Des. 2018, 18, 4306−4319

and $\omega_{\alpha,0} = 0$ ($\omega_{\beta,0}$ is not shown here, but it is nonzero). Now consider the pure α curves (red). For each value of A_β reported, the value of y at the pure α steady state increases as A_α increases. This is expected because agglomeration events reduce surface area. As agglomeration becomes more prevalent in the MSMPR precipitator, the average crystal size increases (due to agglomeration) and the total (distribution integrated) surface area decreases. Crystals grow from the surface, so increasing agglomeration tends to lower the total solute deposition rate from solution, thereby pushing C closer to C_0 and increasing the dimensionless reactor supersaturation (y). A bifurcation occurs at a critical value of A_α (designated $A_\alpha^{crit} \approx 0.5$ in this example), at which point a new, mixed-polymorph steady state becomes possible and dynamically stable for $A_\alpha > A_\alpha^{crit}$. All of our calculations indicate that this bifurcation occurs at the value of A_α for which the steady state value of y is the same at both the pure α steady state and the pure β steady state in the limit $A_\beta = 0$ (i.e., the set of parameters for which $y_{\alpha,A\alpha\neq0} = f(\mathrm{Da}_\alpha, g_\alpha, b_\alpha, \gamma, A_\alpha) = y_{\beta,A\beta=0} = g(\mathrm{Da}_\beta, g_\beta, b_\beta)$). This observation is consistent with the calculations shown here, and with all similar calculations we have performed while studying this system.

Although A_α^{crit} is the same for all A_β at fixed values of Φ_α and Φ_β, the value of A_β does affect the quantitative values of the states at the mixed-polymorph steady state when $A_\alpha > A_\alpha^{crit}$. In fact, one can tell from these diagrams that increasing either of the Agglomeration numbers at fixed values of the other parameters tends to direct the quantitative value of each of the states at the mixed-polymorph steady state toward the value each would have at the opposite form pure steady state. For example, in Figure 2a–c, the values of the mixed polymorph $\omega_{\alpha,0}$ (blue) approach the pure α curve (red) as A_β is increased. In other words, the mixed-form distribution approaches a pure α distribution as A_β increases. This is again consistent with the fact that increasing the importance of agglomeration results in a lower *total* growth rate of a given solid form. Similar trends are observed in the y vs A_α curves for both the mixed-polymorph steady state and the pure α steady state. The solute concentration at the mixed-polymorph steady state approaches the quantitative value associated with the pure β steady state as A_α increases. Similarly, the solute concentration at the pure α steady state approaches the quantitative value associated with the trivial steady state as A_α increases. Both trends are again consistent with the fact that higher A_α slows the *total* α growth rate. Lowering the *total* α growth rate at fixed β parameters evolves the mixed-polymorph steady state toward the pure β steady state and the pure α steady state toward the trivial steady state.

Numerical Stability Analysis. The linear stability analysis performed on the previous model is not possible on the more complicated agglomerating model. Nevertheless, many of the findings from the nonagglomerating model can be applied to the numerical analysis of the agglomerating model. For example, several of the lines in parameter space that served as stability limits and bifurcations in the simpler model can be extended into the agglomeration dimensions, generating stability transition surfaces in higher dimensions. These similarities will be discussed after describing our numerical approach to analyzing the highly nonlinear, agglomerating crystallizer model.

Stability transitions in the full agglomerating model are summarized in Figure 3. These figures were generated numerically by solving the full model for many different values

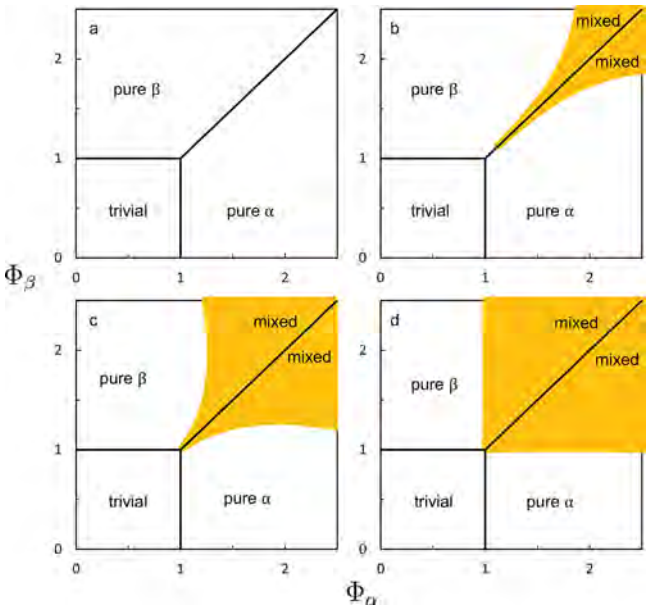

Figure 3. Plots of Φ_β versus Φ_α for the Agglomeration numbers, $A_\alpha = A_\beta$ = (a) 0, (b) 0.1, (c) 1.5, and (d) 150. Each point represents a potential process with a set of relative rates defined by the dimensionless groups (Φ_α, Φ_β, A_α, and A_β). These stability diagrams illustrate the relationships among the relative rates (dimensionless groups) and the relative steady state dynamic stabilities of the four qualitatively distinct steady states. The region of parameter space characterized by the relative dynamic stability of the mixed-polymorph steady state is shaded yellow. This region exists only along the $\Phi_\alpha = \Phi_\beta$ line when $A_i = 0$. It emanates from this line in either direction as the Agglomeration numbers increase, and it covers the entire region described by eqs 34 and 35 in the limit $A_\alpha = A_\beta \rightarrow \infty$. Figure 3a–d were calculated with $\gamma = -0.0042$ (the value associated with the experiments described in Figure 5), $g_i = 1.5$, and $b_i = 2.5$ (generally representative of many systems).

of the 9 parameters. Each transient was evolved until the time derivatives of the moment and mass balance ODEs became zero (with "zero" defined as <0.0001). Then the resulting (stable) state vector was associated with one of the qualitative steady states (trivial, pure α, pure β, or mixed). The data are presented as projections of the nine-dimensional parameter space onto the two-dimensional stability parameter space defined by Φ_α and Φ_β. This presentation represents all of the stability transitions exactly when $A_\alpha = A_\beta = 0$ (see Figure 3a). It remains useful even when $A_i \neq 0$, because many of the general stability transitions can be described in terms of the two stability parameters (Φ_α and Φ_β) alone, and even the higher dimensional bifurcation surfaces become weak functions of the other parameters when presented in this way.

For example, neither the stability transition from the trivial steady state to the pure α steady state nor the transition from the trivial state to the pure β steady state is a function of the Agglomeration numbers (see Figures 1 and 3). The trivial steady state is linearly stable when

$$\Phi_\alpha < 1 \tag{28}$$

$$\Phi_\beta < 1 \tag{29}$$

This is unchanged from the previous, nonagglomerating model. Also similar to the previous nonagglomerating model, both surfaces in parameter space defined by $\Phi_\alpha = 1$, $\Phi_\beta \in [0, 1]$, $A_\alpha \in [0, \infty)$ and $\Phi_\beta = 1$, $\Phi_\alpha \in [0, 1]$, $A_\beta \in [0, \infty)$ separate

DOI: 10.1021/acs.cgd.8b00116
Cryst. Growth Des. 2018, 18, 4306–4319

the region of stable trivial steady states from the regions characterized by the dynamic stability of either the pure α or pure β steady state, respectively. Independent of Agglomeration numbers, the pure α steady state is always dynamically stable when

$$\Phi_\alpha > 1 \tag{30}$$

$$\Phi_\beta < 1 \tag{31}$$

and the pure β steady state is always dynamically stable when

$$\Phi_\alpha < 1 \tag{32}$$

$$\Phi_\beta > 1 \tag{33}$$

(see Figures 1 and 3). These relationships would be difficult to establish from the nine-dimensional numerical data without the guidance provided by the analytic results from our earlier study.[21] These past results enabled us to hypothesize that the stability transitions in the Φ_α–Φ_β plane that exist when $A_i = 0$ may remain independent of A_i for the case $A_i \neq 0$. This hypothesis was tested and confirmed for the trivial to pure α and trivial to pure β transitions with the numerical approach described above. Equations 34 and 35 define the remaining region of parameter space. This is the only region of parameter space in which the steady state dynamic stability is affected by the Agglomeration numbers.

$$\Phi_\alpha > 1 \tag{34}$$

$$\Phi_\beta > 1 \tag{35}$$

In the absence of agglomeration ($A_\alpha = A_\beta = 0$, Figure 3a), the dynamic stability of this region is entirely determined by the relative magnitudes of Φ_α and Φ_β. When $\Phi_\alpha > \Phi_\beta$, the pure α steady state is dynamically stable and when $\Phi_\alpha < \Phi_\beta$, the pure β steady state is dynamically stable. In the absence of agglomeration, mixed-polymorph steady states are only possible along the line $\Phi_\alpha = \Phi_\beta$. A steady state that is only possible along a line in parameter space cannot be observed experimentally (infinitesimal variations or disturbances in any parameter result in departures from the exact operating conditions necessary to maintain one's position on the line), so we deemed it unworthy of substantial discussion in our previous paper. This transition line becomes a transition region in the presence of agglomeration, enabling the observation of these mixed polymorph steady states. The region of mixed-polymorph dynamic stability emanates from this line as the Agglomeration numbers increase (see Figures 3b, c) and eventually covers the entire region defined by eqs 34 and 35 in the limit $A_\alpha, A_\beta \to \infty$ (see Figure 3d).

For each figure shown, g_α, b_α, g_β, b_β, and γ were fixed, and Da_α and Da_β were manipulated to vary Φ_α and Φ_β. This procedure was repeated for several fixed values of A_α and A_β. Away from the limits of $A_i \approx 0$ and $A_i \approx \infty$, most of the variations in the mixed-polymorph/pure polymorph bifurcation surfaces as functions of the parameters (and all of the variation in the other bifurcation surfaces) can be explained by these four parameters alone. In fact, when the stability results are projected onto this two-dimensional stability plane (as in Figure 3), the surface projection characterized by $\Phi_\alpha > \Phi_\beta$ only depends on A_α, γ, g_α, and b_α, while the surface projection characterized by $\Phi_\alpha < \Phi_\beta$ only depends on A_β, g_β, and b_β. Additional discussion of where the bifurcation surfaces generally exist within parameter space and of the (relatively small) movement of the bifurcation surfaces due to changes in the other parameters (γ, g_i, and b_i) is in the Supporting Information. The two intermediate values of $A_\alpha = A_\beta = 0.1, 1.5$ in Figure 3b,c were chosen to represent moderate and high Agglomeration numbers. Figure 3d, where $A_i = 150$, is included as a proxy for the limit as $A_i \to \infty$, but its inclusion is not meant to imply that Agglomeration numbers of this magnitude are attainable. Figure 3 is intended to be as representative as possible of the $CaCO_3$ experiments presented in this article, but it is difficult to exactly define the bifurcation surfaces in this system due to the lack of relevant kinetic data. However, the positions of the bifurcation surfaces (with respect to the stability parameters, Φ_i) are weak functions of the unknown parameters, and these parameters are physically well-constrained. Thus, these limitations barely reduce the utility of the analysis.

From the above analysis, much can be learned and applied to the production of vaterite. First, outside the mixed-polymorph stability region, the dynamic stability features of this model are remarkably similar to those of the nonagglomerating model. A region of trivial steady state dynamic stability remains, characterized by low residence times relative to the nucleation and growth times of both forms. Regions of parameter space also exist in which one expects to observe pure calcite and pure vaterite steady states. Second, the region in which the mixed-polymorph steady state is dynamically stable is localized around the original bifurcation line ($\Phi_\alpha = \Phi_\beta$). Third, the mixed-polymorph stability region grows as the Agglomeration numbers increase. These three observations provide enough information to design polymorph selective processes for agglomerating precipitators. Observation 2 implies that by holding A_α and A_β constant, one can decrease the relative stability of the mixed-polymorph steady state by moving orthogonally away from the $\Phi_\alpha = \Phi_\beta$ line. Observation 3 implies that by holding Φ_α and Φ_β constant, one can destabilize the mixed-polymorph steady state by decreasing A_α or A_β. Combining these two observations, any design or operation decision that moves the process toward lower Agglomeration numbers or away from the $\Phi_\alpha = \Phi_\beta$ line will tend to destabilize the mixed-polymorph steady states in favor of the pure form steady states. The pure form steady state that this change will stabilize will depend on the relative magnitudes of Φ_α to Φ_β, i.e., on which side of the $\Phi_\alpha = \Phi_\beta$ line the operating point falls.

In general, most of the model parameters (dimensionless groups) vary as functions of temperature (T). Therefore, the stability parameters (Φ_α and Φ_β) are also functions of temperature. This implies that changing temperature (while holding all other decision variables constant) changes the relative values of both the stability parameters (Φ_i) and the Agglomeration numbers (A_i), moving an operating point around Figure 3. For some changes in temperature, a different steady state will become dynamically stable. If one can characterize the growth kinetics, nucleation kinetics, and solubilities of both forms as functions of temperature, then temperature becomes a valuable decision variable to use for polymorph selection.

The inlet concentration (C_0) is another design choice that can be used to select the relative values of the stability groups and the Agglomeration numbers, and accordingly, the steady state solid form produced. System-specific nucleation and growth rate expressions are required to define the exact relationships between inlet concentration, the stability groups,

DOI: 10.1021/acs.cgd.8b00116
Cryst. Growth Des. 2018, 18, 4306–4319

and the Agglomeration numbers, but scaling arguments can be used to make intentional design decisions in systems for which the kinetics have not yet been characterized. For example, the stability groups increase linearly with increases in the inlet concentration, and the Agglomeration numbers decrease by the nonlinear scaling $A_i \approx C_o^{-(3g_i-1)}$ (see eqs 15−18 and 26 and 27). Typically, the quantity $3g_i - 1 \approx 5$ and system-specific knowledge is unnecessary to bound the quantity between 2 and 5 because g_i typically varies between 1 and 2. Therefore, Agglomeration numbers decrease at a rate between C_o^{-2} and C_o^{-5}. This nonlinear Agglomeration number decay, coupled with the linear increases of Φ_α and Φ_β, is enough information to accomplish polymorph selection in many systems, even if the exact nucleation and growth kinetics (and therefore the exact functional forms of $\Phi_i = f_\Phi(C_0)$ and $A_i = f_A(C_0)$) are unknown. Increasing C_o has a larger effect on shrinking the region of mixed-polymorph dynamic stability than it does in affecting the relative polymorphic nucleation and growth rates that move an operating point around the $[\Phi_\alpha, \Phi_\beta]$ plane. For example, doubling the inlet concentration decreases the Agglomeration numbers by a factor between 4 and 32. Since typical Agglomeration numbers vary between 0 and 1.5, and since Figure 3b illustrates how small the mixed-polymorph region becomes for $A_i \leq 0.1$, a small increase in the inlet concentration will have a relatively large effect on shrinking the mixed-polymorph stability region and a relatively small effect on the relative dynamic stability of the pure polymorph steady states. Furthermore, if a set of design choices is known to yield a mixed-polymorph steady state for which the more prevalent form is desired (as in Figure 5), one could reasonably conclude that the system is in a position on the stability diagram for which $\Phi_{\text{desired}} > \Phi_{\text{undesired}}$. Therefore, a hypothesis emerges from these scaling arguments: one can design a polymorph selective process for an agglomerating crystal system by using the design rules from the nonagglomerating model while maintaining a high inlet supersaturation.

Similar scaling arguments also apply to residence time (τ). The Φ_i scale as $\tau^{3/(2g_i+b_i)}$ and the Agglomeration numbers scale as τ^{-2}. The quantity $3/(2g_i + b_i) \in [0, 1]$, so increasing residence time is also a reasonable approach when attempting to destabilize a mixed-polymorph steady state. Still, increasing C_0 is likely a better option to try first for two reasons. First, the difference in scaling between the Φ_i and the A_i is typically larger for C_0, indicating that the destabilizing effect should be more effective for a smaller change in C_0 (and therefore a smaller displacement in the $[\Phi_\alpha, \Phi_\beta]$ plane). Furthermore, we demonstrated in our earlier study that increasing residence time always increases the relative value of the thermodynamically stable solid form's stability group to the thermodynamically metastable solid form's stability group. Therefore, a large enough increase in residence time is guaranteed to give a pure, thermodynamically stable solid form at steady state. For some applications, that may be ideal, but for our motivating system of vaterite precipitation, increasing C_0 is a superior design choice. Still, Figure 5a,b illustrates that the relative fraction of vaterite increased when the residence time was increased, indicating that both strategies could be effective in this system.

EXPERIMENTAL SECTION

Materials and Apparatus. Experiments were performed in a 1 L LabMax reactor (Mettler Toledo, see Figure 4). The reactor temperature was controlled to 25 °C. Inlet and outlet flows were calibrated to maintain an active reactor volume in the range of 0.2−0.6 L, so that the residence time could be varied between 6 and 18 min. During each experiment, two separate equimolar (stoichiometric) flows of aqueous Na_2CO_3 and $CaCl_2$ were fed to the MSMPR reactor. The 99%+ purity solid reactants were purchased from Fisher Chemical, and used as-received. The water used to generate the aqueous feed solutions was filtered in a Barsted NANOpure water filtration system with a conductivity of 18 $\mu\Omega$ cm^{-1}. As two separate equimolar streams were fed to the reactor, the inlet concentration as defined in the model (C_0) is one-half the molar concentration in either feed stream (see Supporting Information for discussion). A set of experimental conditions were repeated to confirm the reproducibility of the experimental procedure (as discussed in the Supporting Information).

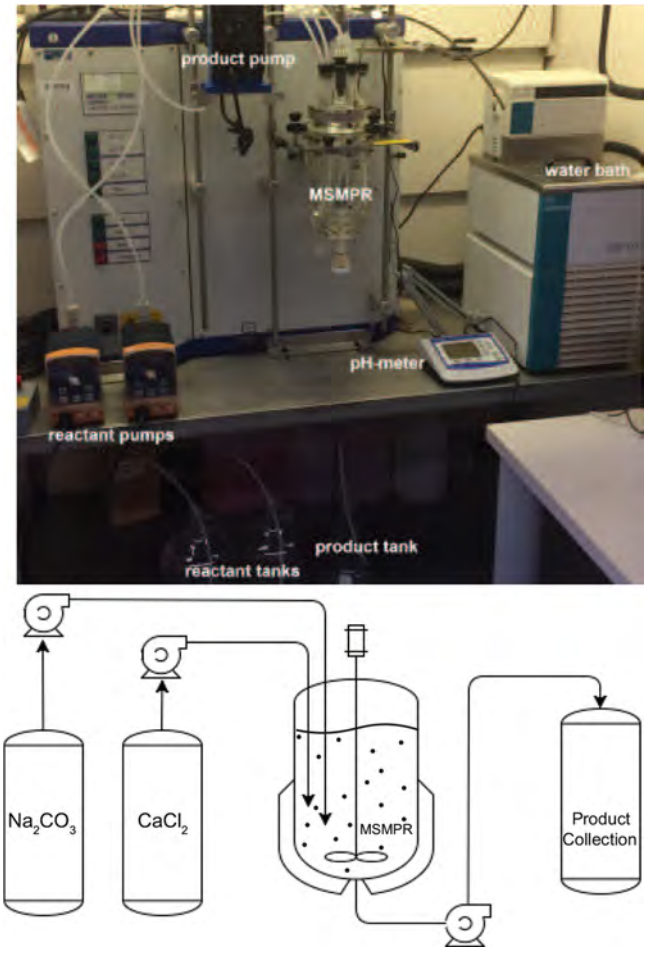

Figure 4. Experimental apparatus (top) and schematic (bottom) for continuous precipitation experiments in which Na_2CO_3 and $CaCl_2$ were converted to $CaCO_3$. Temperature was controlled to 25 °C for all experiments. The inlet concentration was varied from 0.0025 to 0.15 molar. The residence time was varied between 6 and 18 min.

Product Characterization. The pH of the solution inside the reactor was measured every 3 s with a Fisher Scientific accumet AB150. Precipitator dynamics were also monitored at discrete 30 min intervals with powder X-ray diffraction on the effluent solids. Steady state was declared when both measurements ceased changing in time (±3% for phase fractions and ±0.01 for pH). The process dynamics can be monitored with pH because the well-understood reaction equilibrium is very pH sensitive (see the Supporting Information for discussion of the chemistry and justification of this procedure). Solid $CaCO_3$ was continuously removed from the reactor in the exit suspension stream and filtered in a Büchner funnel with a 0.3 μm filter. The solids were then dried in an oven for 24 h at 70 °C before further characterization.

DOI: 10.1021/acs.cgd.8b00116
Cryst. Growth Des. 2018, 18, 4306−4319

Complementary powder X-ray diffraction (XRD), solid-state ^{43}Ca nuclear magnetic resonance spectroscopy (NMR), and electron microscopy (SEM) analyses were used to characterize the local and long-range order, compositions, and morphologies of the crystallization products. Powder XRD patterns were acquired under several different drying procedures to confirm that the described drying process did not alter the polymorph distribution (see Supporting Information for details.) Once dry, XRD patterns of the solid products were acquired on an Empyrean Powder Diffractometer, and phase-fitting of the pattern was completed in Highscore (PANalytical XRD analysis software). Select samples were also characterized with scanning electron microscopy (SEM) on a FEI Nova Nano 650 FEG SEM. Characterization of ^{43}Ca is difficult due to its low gyromagnetic ratio (-1.803×10^7 rad T^{-1} s^{-1}), low natural isotopic abundance ($\approx$ 0.135%), and the general difficulties associated with quadrupolar nuclei (7/2 spin). These challenges were mitigated with high magnetic fields (19.6 T) and a custom-built 7 mm single-resonance probe specifically designed for low-γ nuclei at the U.S. National High Magnetic Field Laboratory in Tallahassee, Florida. Solid-state, single-pulse ^{43}Ca magic-angle-spinning (MAS) NMR spectra of select samples were acquired on a 19.6 T Bruker DRX NMR spectrometer under magic-angle-spinning (MAS) conditions of 5 kHz, 25 °C, 90° 4 μs pulses, and a 0.5 s recycle delay. The ^{43}Ca shifts were referenced to 1 molar aqueous $CaCl_2$. Additional diffraction patterns and solid-state ^{43}Ca NMR spectra are included in the Supporting Information, including a ^{43}Ca NMR spectrum of a sample containing calcite, vaterite, and aragonite phases,which shows resolved ^{43}Ca signals from each phase. The peaks are centered at 20 ppm, 3 ppm, and −27 ppm, but the exact location of the peaks is sensitive to the reference concentration chosen.[45]

RESULTS AND DISCUSSION

Evidence of Mixed Polymorph Steady States. Mixed-polymorph steady states are often observed during the continuous precipitation of $CaCO_3$, but these steady states are not possible solutions to population balance models for which the dominant rate processes are secondary nucleation and size-independent linear crystal growth alone.[21] We have demonstrated (using arc-length continuation and a numerical stability analysis) that mixed-polymorph steady states are possible and even dynamically stable for some agglomerative precipitation process models. In this section, we discuss two experiments for which such mixed-polymorph steady states were observed. These experiments were performed with a stoichiometric feed of Na_2CO_3 and $CaCl_2$ at a concentration (C_0) of 0.0125 molar and a temperature (T) of 25 °C. The residence times (τ) were 6 and 9 min for Figure 5a and b, respectively. The percentage of the effluent solids that was associated with each polymorph at each time point was determined using powder X-ray diffraction and Rietveld phase fitting. For example, Figure 5 illustrates how the effluent crystal polymorph distribution changed as a function of time during these two experiments (% polymorph defined as mass of solid form i/total mass of solids ×100%). In Figure 5a,b, the polymorph distributions vary with time during start-up but eventually plateau, indicating that a steady state has been reached. In each case, the crystal distribution leaving the precipitator at steady state contains nonzero amounts of both calcite and vaterite polymorphs (75% vaterite for τ = 6 min and 93% vaterite for τ = 9 min), indicating that some rate process besides size-independent linear crystal growth and secondary nucleation must be important.

Figure 6 shows typical SEM images of the effluent crystals after filtration and drying. Figure 6a is an image of product crystals collected after 30 min of operation for T = 25 °C, C_0 = 0.0125 M, and τ = 9 min (Figure 5b) . After 30 min, the process was still exhibiting start-up dynamics ($\approx$ 42% calcite), resulting in a mixture of calcite (cube-like) and vaterite (spheroidal) crystallites. A significant extent of crystal

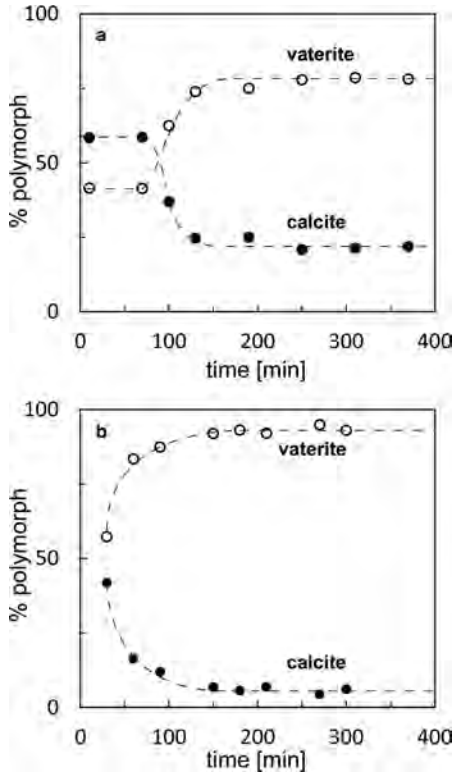

Figure 5. Percentages of the different $CaCO_3$ polymorphs plotted as functions of time during continuous precipitation for T = 25 °C, C_0 = 0.0125 M, and (a) τ = 6 min, or (b) τ = 9 min. Both vaterite (thermodynamically metastable) and calcite (thermodynamically stable) coexist at steady state in both experiments. These are typical experiments that exhibit a dynamically stable mixed-polymorph steady state.

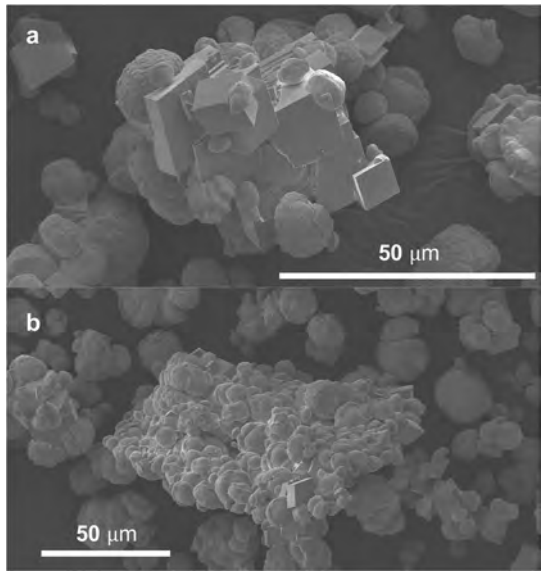

Figure 6. Representative SEM images of effluent cube-shaped calcite crystallites and spheroidal vaterite crystallites after (a) 30 min and (b) 60 min of start-up of a continuous $CaCO_3$ precipitation experiment operating at T = 25 °C, C_0 = 0.0125 M, and τ = 9 min. Both images exhibit mixed-polymorph distributions and significant agglomeration.

DOI: 10.1021/acs.cgd.8b00116
Cryst. Growth Des. 2018, 18, 4306−4319

agglomeration is also observed. Figure 6b is a representative image collected after 60 min of operation for T = 25 °C, C_0 = 0.0125 M, and τ = 9 min. This point in the start-up dynamics is closer to the steady state distribution and therefore exhibits a relatively low calcite fraction (16%). Again, the image clearly shows that both solid forms are present along with significant agglomeration.

Testing the Hypothesis. The previously discussed analysis indicated that increasing the inlet concentration (C_0), while holding all other decision variables constant with respect to the experiment described in Figure 5a, should have a destabilizing effect on the mixed-polymorph steady state in favor of the pure vaterite steady state. Figure 7 illustrates how

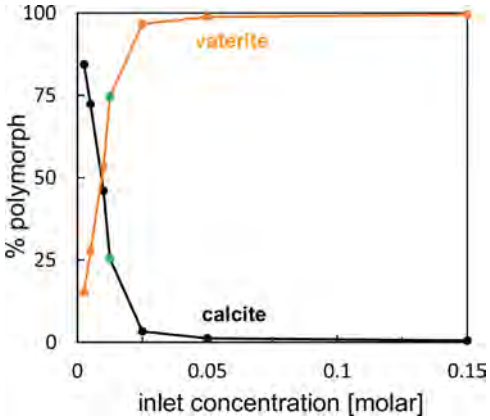

Figure 7. Plots of the steady state percentage of vaterite and calcite polymorphs obtained for various values of C_0 at fixed values of τ (6 min) and T (25 °C). As the inlet concentration is increased, the fraction of effluent crystals identified as vaterite increases and eventually approaches 100%. The green points indicate the steady state polymorph distribution associated with the experiment described in Figure 5a.

the steady state values of the different polymorph percentages changed as a function of C_0 at the fixed residence time (6 min) and temperature (25 °C) corresponding to the conditions used in Figure 5a. When C_0 = 0.0125 molar, the steady state distribution contained approximately 75% vaterite and 25% calcite (green points). When C_0 was increased by a factor of 12 to C_0 = 0.15 molar, the steady state percentage of vaterite approached 100%. These $CaCO_3$ data indicate that increasing inlet supersaturation decreases the relative importance of agglomeration inside the continuous MSMPR precipitator, thereby destabilizing the mixed-polymorph steady state in favor of a pure polymorph steady state.

Characterization of the effluent products establishes that for τ = 6 min, T = 25 °C, and C_o = 0.15 M, the thermodynamically metastable polymorph, vaterite, is almost exlcusively present. Figure 8 shows a powder X-ray diffraction pattern (XRD), a solid-state ^{43}Ca NMR spectrum, and two SEM images of these effluent solids. All of the major reflections in the XRD pattern are indexable to vaterite, although a minor reflection exists that may be indexable to calcite (<1%). The solid-state ^{43}Ca MAS NMR spectrum in Figure 8b shows a broad signal centered at 3 ppm that is assigned to Ca^{2+} ions in a distribution of local vaterite environments.[46,47] An additional ^{43}Ca MAS NMR spectrum acquired on a solid mixture of calcite, vaterite, and aragonite under otherwise identical conditions is included in the Supporting Information. This additional spectrum shows two additional ^{43}Ca peaks. In Figure 8b, there is no observable NMR signal at either 20 ppm (calcite) or −27 ppm (aragonite), indicating that the sample is predominately vaterite. Furthermore, the representative SEM images in Figure 8c,d show only spheroidal vaterite crystallites with no cube-shaped calcite crystallites present.

The agglomeration prevalent in the SEM images highlights an important point. Increasing the inlet concentration does not necessarily lower the agglomeration rate. In fact, nonconstant agglomeration kernels (β_i) are known to increase as supersaturation increases.[28,48,49] The important distinction is that the agglomeration kernel (β_i) is only one component of the Agglomeration number (A_i), and it is this Agglomeration number that affects the steady state dynamic stability. The Agglomeration number depends on β_i, but it also depends on the crystal growth kinetics and the residence time. In this case, increasing the inlet concentration lowered the Agglomeration number and destabilized the mixed polymorph steady state, even though the absolute agglomeration frequency likely increased.

Other Polymorphic Systems. The previous polymorph selection design rules were constructed to be generally applicable to any bipolymorphic system in which size-independent linear crystal growth and secondary nucleation are the dominant rate processes. The design rules were tested for specific crystal systems for which relevant experiments had been reported in the literature (e.g., L-glutamic acid and *p*-aminobenzoic acid[21]). These analyses were carried out under the implicit assumption that agglomeration was unimportant in these systems, and the design rules generated in this way were consistent with the reported experimental results. Now that the effect of agglomeration on steady state dynamic stability during continuous precipitation has been demonstrated to be important in some systems, we revisit the previous assumptions and results, specifically taking into account the agglomeration kinetics in the L-glutamic acid system.

Using the expressions from Lindenberg et al.,[48] we estimate the size-independent α form agglomeration kernel (β_α) to be in the range of $3.6 \times 10^{-12} - 6.5 \times 10^{-12}$ m^3/s, depending on the experimental conditions. These are relatively high values for β: for example, β is on the order 10^{-17} for calcium oxalate,[50] 10^{-14} for $CaCO_3$,[51] and general hydrodynamic approximations in the high growth rate and high collision frequency limit are 10^{-18}–10^{-16}.[52] A relatively high value of β_α suggests that agglomeration could be important in this system; however, the physicochemically important quantity is the dimensionless Agglomeration number (A_α), which is also affected by the growth kinetics and the residence time.

The Agglomeration number can be estimated for the four L-glutamic acid experiments that were reported by Lai et al. and discussed in our previous paper by taking the agglomeration kinetics from Lindenberg et al. and the growth kinetics from Lai et al.[19,21,48] The relevant experiments were numbered 1−4 and described in Table 1 in Lai et al.[19] During each experiment, L-glutamic acid was continuously crystallized to give pure steady state distributions of the thermodynamically metasatable α-polymorph at a temperature of 25 °C and a feed concentration of 40 g/kg. The residence time was varied from 30 to 120 min in equal increments. Taking the maximum agglomeration frequency rate coefficient from our estimated range ($\beta_\alpha = 6.5 \times 10^{-12}$), the Agglomeration numbers associated with these four experiments are 0.148, 0.028, 0.011, and 0.005, respectively. Figure 9 shows the outer

DOI: 10.1021/acs.cgd.8b00116
Cryst. Growth Des. 2018, 18, 4306−4319

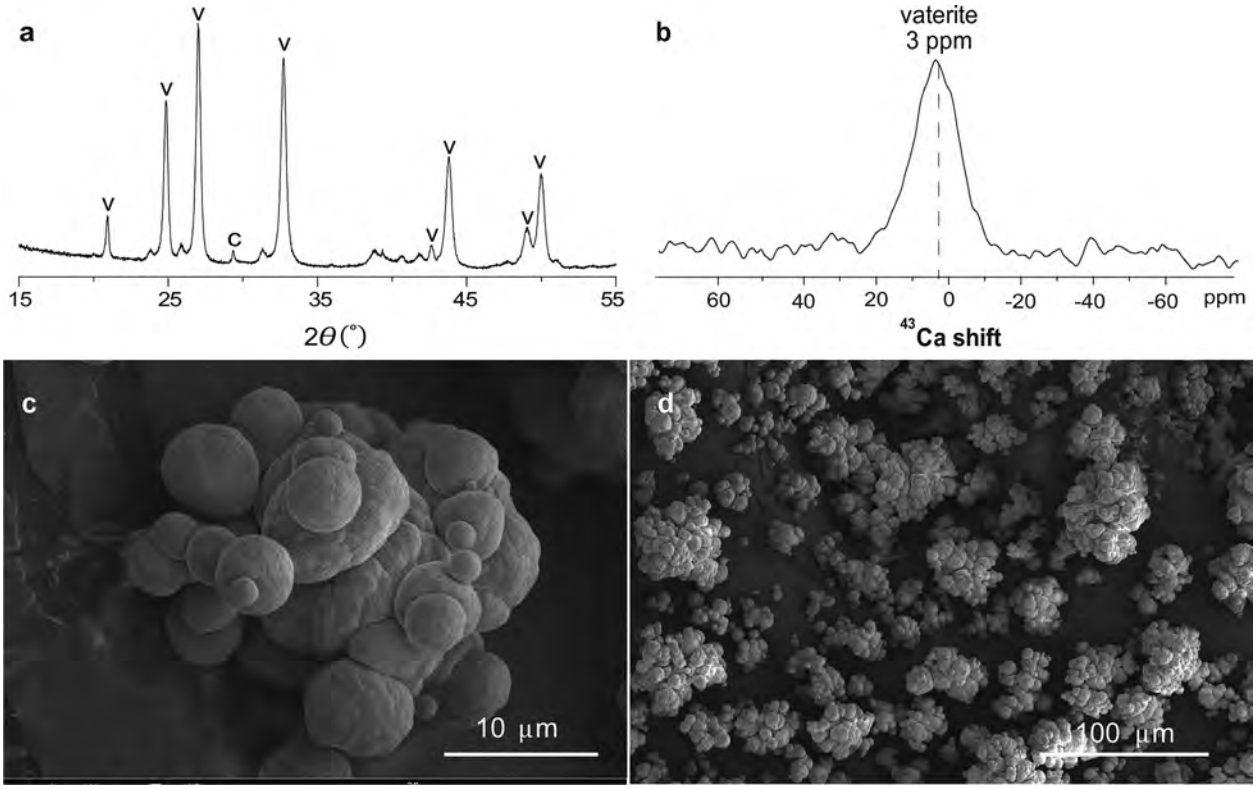

Figure 8. (a) Powder X-ray diffraction pattern, (b) solid-state, single-pulse ^{43}Ca MAS NMR spectrum, and (c,d) SEM images. Product collected from a continuous precipitation experiment operating under steady state conditions, a residence time (τ) of 6 min, a temperature (T) of 25 °C, and an inlet concentration (C_0) of 0.15 molar. All major reflections in the XRD pattern are indexable to vaterite, although a minor reflection may be indexable to calcite (<1%). The ^{43}Ca MAS NMR spectrum was acquired at 19.6 T, 25 °C, 5 kHz MAS, and required a 47.6 h acquisition time, yielding a single peak centered around 3 ppm. The spheroidal crystallites in (c) and (d) are consistent with vaterite.

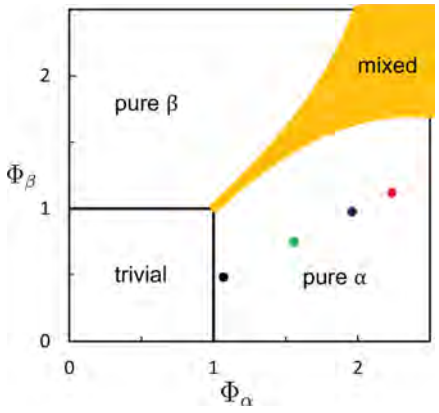

Figure 9. Stability diagram for L-glutamic acid, in which Φ_β (thermodynamically stable form) is plotted versus Φ_α (thermodynamically metastable form) with parameter regions labeled to indicate the steady state that is predicted to be dynamically stable in each region. The mixed-polymorph dynamic stability region is shaded yellow for $A_\alpha = A_\beta = 0.148$. This is the highest Agglomeration number of all of the L-glutamic acid experiments considered in our previous publication (experiments originally reported in Lai et al.).[19,21] The experiments were performed at 25 °C, C_0 = 40 g/kg, and τ = 30 (black), 60 (green), 90 (blue), and 120 min (red). For this figure, γ = −0.07, g_α = 1.31, b_α = 2.62, g_β = 1.10, and b_β = 2.81, consistent with the calculations discussed in our previous article.[21] The polymorphically pure, thermodynamically metastable, polymorph (α) is predicted by the agglomeration-enabled design rules and also observed experimentally.

envelope of the mixed-polymorph dynamic stability region defined for $A_\alpha = A_\beta = 0.148$. The ordered pairs $[\Phi_\alpha, \Phi_\beta]$ associated with the same experiments are also included on Figure 9 to illustrate that these experiments were not near the mixed-polymorph/pure α polymorph dynamic stability boundary. These calculations support the assumptions in the previous analysis and support the simpler theoretical treatment that is typically used in the L-glutamic acid system.

While the motivating application for this work was $CaCO_3$ precipitation, the model and the analysis are general and can be expected to apply to other agglomerative precipitations. For other systems with different nucleation, growth, and agglomeration kinetics, one can use Figure 3 to interpolate an approximate mixed-polymorph/pure-polymorph bifurcation surface. We expect that most systems will exhibit Agglomeration numbers in the range of 0−1.5. As one can see from Figure 3c,d, A_i = 1.5 is already qualitatively similar to the $A_i \rightarrow \infty$ limit, so most interpolations should be possible with just Figure 3 alone. To further facilitate this type of interpolation for other systems, we have provided additional numerical results in the Supporting Information with alternate combinations of γ, g_i, and b_i.

CONCLUSION

Differences in crystal structure imply and typically correlate to differences in measurable macroscopic properties. These properties often have a significant impact on a material's utility for a given application, and therefore a preferred solid form usually exists when one designs an industrial crystallizer or precipitator. Previously developed polymorph selection

DOI: 10.1021/acs.cgd.8b00116
Cryst. Growth Des. 2018, 18, 4306−4319

design rules did not account for crystal agglomeration, so a new approach was required to develop polymorph selective precipitators for the $CaCO_3$ system. Here, we have shown that agglomeration changes the relative dynamics within the crystallizer/precipitator, thereby affecting the relative dynamic stability of the four competing steady states. The new design rules presented here can be utilized to direct solid form during agglomerative precipitations, even if the preferred solid form is thermodynamically metastable. Pure, thermodynamically metastable, technologically preferred, vaterite ($CaCO_3$) crystal distributions have been produced in accordance with the process conditions indicated by the model analysis presented here.

Each of the three systems that have experimentally corroborated the polymorph selection design rules presented here and in our earlier paper are capable of exhibiting two crystalline polymorphs near experimental conditions. The two-polymorph case has been explicitly modeled and analyzed here, but the conclusions are expected to be broadly applicable to noncrystalline and multipolymorph systems. The model equations and analysis are expected to apply to noncrystalline forms because the rate expressions that govern the nucleation, growth, and agglomeration of noncrystalline forms are similar to the expressions that govern crystalline forms. The arguments and conclusions are also anticipated to apply to systems capable of exhibiting more than two solid forms over a range of experimental conditions. In fact, several other solid forms of $CaCO_3$ are possible at slightly higher and lower temperatures. We expect that additional analysis and kinetic characterization of the $CaCO_3$ system will yield a higher dimensional version of Figure 2 that one could utilize to select conditions for precipitating any of these solid forms.

■ ASSOCIATED CONTENT

Supporting Information

The Supporting Information is available free of charge on the ACS Publications website at DOI: 10.1021/acs.cgd.8b00116.

Summary of $CaCO_3$ chemistry; model details and analysis; agglomeration kernel; discussion of the functional form of the Damköhler numbers; non-stoichiometric feed and non-dimensionalization; crystal drying procedure; reproducibility; NMR spectra and XRD patterns; vaterite stability data; nucleation rate expression pre-factor (PDF)

■ AUTHOR INFORMATION

Corresponding Author

*E-mail: mfd@ucsb.edu.

ORCID

Thomas C. Farmer: 0000-0002-8970-7023

Bradley F. Chmelka: 0000-0002-4450-6949

Michael F. Doherty: 0000-0003-3309-3082

Present Address

‡Technical University of Munich, Munich, Germany

Notes

The authors declare no competing financial interest.

■ ACKNOWLEDGMENTS

We thank Dr. Z. Gan and N. Prisco for assistance with the solid-state ^{43}Ca MAS NMR measurements, which were conducted at the NSF-supported U.S. National High Magnetic Field Laboratory in Tallahassee, Florida. We also thank Amgen for donating the LabMax reactor in which the experiments reported here were performed. The authors acknowledge the U.S. National Science Foundation (Award No. CBET-1335694) for support of this work.

■ NOTATION

n_i (number/volume/length)	particle density of polymorph i
G_i(length/time)	growth rate of polymorph i
x (length)	crystal length coordinate
β_i (volume/number/time)	polymorph i agglomeration frequency rate coefficient
τ (time)	MSMPR residence time
B_i (number/(volume-time))	nucleation rate of polymorph i
C (mol/volume)	solute concentration
$k_{i,g}$ (length/time)	rate constant in growth rate expression
$k_{i,b}$ (number/length^2/time)	rate constant in birth rate expression
ρ (mol/volume)	molar density
$\mu_{i,l}$ (number/volume)	weight l of form i quadrature rule
L_j (length)	length or abscissa in the quadrature rule
$m_{i,0}$ (number/volume)	zeroth moment of polymorph i population
$m_{i,1}$ (length/volume)	first moment of polymorph i population
$m_{i,2}$ (length^2/volume)	second moment of polymorph i population
$\omega_{\alpha,j}$ (dimensionless)	dimensionless jth moment of α population
$\omega_{\beta,j}$ (dimensionless)	dimensionless jth moment of β population
y (dimensionless)	dimensionless concentration
$K_{eq,i}$ (moles^2/volume^2)	equilibrium/solubility constant for solid form i

■ REFERENCES

(1) Thun, J.; Seyfarth, L.; Butterhof, C.; Senker, J.; Dinnebier, R. E.; Breu, J. Wohler and Liebig revisted: 176 Years of Polymorphism in Benzamide-and the Story Still Continues! *Cryst. Growth Des.* **2009**, *9*, 2435−2441.

(2) Ostwald, W. Studien uber die Bildung und Umwandlung fester Korperr. *Z. Phys. Chem.* **1897**, *22*, 289−330.

(3) Cardew, P. T.; Davey, R. J. The Kinetics of Solvent-Mediated Phase Transformations. *Proc. R. Soc. London, Ser. A* **1985**, *398*, 415−428.

(4) Scholl, J.; Lindenberg, C.; Vicum, L.; Brozio, J.; Mazzotti, M. Precipitation of a L-glutamic Acid: Determination of Growth Kinetics. *Faraday Discuss.* **2007**, *136*, 247−264.

(5) Ferrari, E. S.; Davey, R. J.; Cross, W. I.; Gillon, A. L.; Towler, C. S. Crystallization in Polymorphic Systems: The Solution-Mediated Transformation of β to α Glycine. *Cryst. Growth Des.* **2003**, *3*, 53−60.

(6) Brittain, H. G. *Polymorphism in Pharmaceutical Solids*; CRC Press, 2009.

(7) Bernstein, J. *Polymorphism in Molecular Crystals*; Oxford University Press, 2008.

(8) Byrn, S. R. *Solid-state Chemistry of Drugs*; Academic Press, 1982.

(9) LLinas, A.; Goodman, J. M. Polymorph Control: Past, Present and Future. *Drug Discovery Today* **2008**, *13*, 198−210.

(10) Cashell, C.; Corcoran, D.; Hodnett, B. K. Control of Polymorphism and Crystal Size of L-glutamic Acid in the Absence of Additives. *J. Cryst. Growth* **2004**, *273*, 258−265.

DOI: 10.1021/acs.cgd.8b00116
Cryst. Growth Des. 2018, 18, 4306−4319

(11) Kee, N. C.; Tan, R. B. H.; Braatz, R. D. Selective Crystallization of the Metastable α-Form of L-Glutamic Acid Using Concentration Feedback Control. *Cryst. Growth Des.* **2009**, *9*, 3044−3051.
(12) Hermanto, M. W.; Chiu, M.; Braatz, R. D. Nonlinear Model Predictive Control for the Polymorphic Transformation of L-Glutamic Acid Crystals. *AIChE J.* **2009**, *54* (12), 3248−3259.
(13) Yang, X.; Sarma, B.; Myerson, A. S. Polymorph Control of Micro/Nano-Sized Mefenamic Acid Crystals on Patterned Self-Assembled Monolayer Islands. *Cryst. Growth Des.* **2012**, *12*, 5521.
(14) Lee, I. S.; Lee, A. Y.; Myerson, A. S. Concomitant Polymorphism in Confined Environment: Implication to Crystal Form Screening. *Pharm. Res.* **2008**, *25*, 960−968.
(15) Kato, T.; Suzuki, T.; Amamiya, T.; Irie, T.; Komiyama, M. Effects of Macromolecules on the Crystallization of $CaCO_3$: the Formation of Organic/Inorganic Composites. *Supramol. Sci.* **1998**, *5*, 411−415.
(16) Gu, C.; Chatterjee, K.; Young, V., Jr.; Grant, D. J. W. Stabilization of a Metastable Polymorph of Sulfamerazine by Structure Related Additives. *J. Cryst. Growth* **2002**, *235*, 471−481.
(17) Simone, E.; Saleemi, A. N.; Tonnon, N.; Nagy, Z. K. Active Polymorphic Feedback Control of Crystallization Processes Using a Combined Raman and ATR-UV/Vis Spectroscopy Approach. *Cryst. Growth Des.* **2014**, *14*, 1839−1850.
(18) Morissette, S. L.; Soukasene, S.; Levinson, D.; Cima, M. J.; Almarsson, O. Elucidation of Crystal Form Diversity of the HIV Protease Inhibitor Ritonavir by High-throughput Crystallization. *Proc. Natl. Acad. Sci. U. S. A.* **2003**, *100*, 2180−2184.
(19) Lai, T.; Ferguson, S.; Palmer, L.; Trout, B. L.; Myerson, A. S. Continuous Crystallization and Polymorph Dynamics in the L-Glutamic Acid System. *Org. Process Res. Dev.* **2014**, *18*, 1382−1390.
(20) Lai, T. C.; Cornevin, J.; Ferguson, S.; Li, N.; Trout, B. L.; Myerson, A. L. Control of Polymorphism in Continuous Crystallization via Mixed Suspension Mixed Product Removal Systems Cascade Design. *Cryst. Growth Des.* **2015**, *15* (7), 3374−3382.
(21) Farmer, T. C.; Carpenter, C. L.; Doherty, M. F. Polymorph Selection by Continuous Crystallization. *AIChE J.* **2016**, *62*, 3505−3514.
(22) Worlitschek, J.; Mazzotti, M. Model-Based Optimization of Particle Size Distribution in Batch-Cooling Crystallization of Paracetamol. *Cryst. Growth Des.* **2004**, *4*, 891−903.
(23) Garside, J. Industrial Crystallization from Solution. *Chem. Eng. Sci.* **1985**, *40*, 3−26.
(24) Kawano, J.; Shimobayashi, N.; Miyake, A.; Kitamura, M. Precipitation Diagram of Calcium Carbonate Polymorphs: Its Construction and Significance. *J. Phys.: Condens. Matter* **2009**, *21*, 1−6.
(25) Constantz, B. R.; Youngs, A.; Holland, T. Reduced-carbon Footprint Concrete Compositions. U.S. Patent 7,815,880. 2010.
(26) Constantz, B. R.; Farsad, K.; Camire, C.; Chen, I. Methods and Compositions Using Calcium Carbonate. U.S. Patent 7,922,809. 2011.
(27) McNaught, A.; Wilkinson, A. *Compendium of Chemical Terminology* **1997**, *4*, 347.
(28) Mullin, J. W. *Crystallization*; Butterworth-Heinemann, Oxford, 1993; Chapter 8.
(29) Fujiwara, M.; Chow, P. S.; Ma, D. L.; Braatz, R. D. Paracetamol Crystallization Using Laser Backscattering and ATR-FTIR Spectroscopy: Metastability, Agglomeration, and Control. *Cryst. Growth Des.* **2002**, *2*, 363−370.
(30) Padia, B. K.; Bhatia, S. K. Multiplicity and Stability Analysis of Agglomeration Controlled Precipitation. *Chem. Eng. Commun.* **1991**, *104*, 227−244.
(31) Ramkrishna, D. *Population Balances: Theory and Application to Particulate Systems in Engineering*; Academic Press, 2000.
(32) Marchisio, D. L.; Vigil, R. D.; Fox, R. O. Quadrature Method of Moments for Aggregation-Breakage Processes. *J. Colloid Interface Sci.* **2003**, *258*, 322−334.
(33) Fredrickson, A. G.; Ramkrishna, D.; Tsuchiya, H. M. Statistics and Dynamics of Procaryotic Cell Populations. *Math. Biosci.* **1967**, *1*, 327−374.
(34) Dandekar, P.; Doherty, M. F. A mechanstic growth model for inorganic crystals: Growth mechanism. *AIChE J.* **2014**, *60*, 3720−3731.
(35) Marchisio, D. L.; Pikturna, J. T.; Fox, R. O.; Vigil, R. D.; Barresi, A. A. Quadature Method of Moments for Population-Balance Equations. *AIChE J.* **2003**, *49*, 1266−1276.
(36) McGraw, R. Description of Aerosol Dynamics by the Quadrature Method of Moments. *Aerosol Sci. Technol.* **1997**, *27*, 255−265.
(37) Gordon, R. G. Error Bounds in Equilibirum Statistical Mechanics. *J. Math. Phys.* **1968**, *9*, 655−663.
(38) Gimbun, J.; Nagy, Z. K.; Rielly, C. D. Simultaneous Quadrature Method of Moments for the Solution of Population Balance Equations, Using a Differential Algebraic Equation Framework. *Ind. Eng. Chem. Res.* **2009**, *48*, 7798−7812.
(39) McGraw, R.; Wright, D. L. Chemically Resolved Aerosol Dynamics for Internal Mixtures by the Quadrature Method of Moments. *J. Aerosol Sci.* **2003**, *34*, 189−209.
(40) Alopaeus, V.; Laakkonen, M.; Aittamaa, J. Numerical Solution of Moment-Transformed Population Balance Equation with Fixed Quadrature Points. *Chem. Eng. Sci.* **2006**, *61*, 4919−4929.
(41) Sampson, K. J.; Ramkrishna, D. A New Solution to the Brownian Coagulation Equation through the Use of Root-Shifted Problem-Specific Polynomials. *J. Colloid Interface Sci.* **1985**, *103*, 245−254.
(42) Strogatz, S. H. *Nonlinear Dynamics and Chaos*; Westview Press, 1994.
(43) Seydel, R. *Practical Bifurcation and Stability Analysis*; Springer Science & Business Media, 2009.
(44) Kubicek, M. Algorithm 502 Dependence of Solution of Nonlinear Systems on a Parameter. *ACM Transactions on Mathematical Software* **1976**, *2*, 98−107.
(45) Bryce, D. L.; Bultz, E. B.; Aebi, D. Calcium-43 Chemical Shift Tensors as Probes of Calcium Binding Environments. Insights into the Structure of the Vaterite $CaCO_3$ Polymorph by ^{43}Ca Solid-State NMR Spectroscopy. *J. Am. Chem. Soc.* **2008**, *130*, 9282−9292.
(46) Demichelis, R.; Raiteri, P.; Gale, J. D.; Dovesi, J. D. The Multiple Structures of Vaterite. *Cryst. Growth Des.* **2013**, *13*, 2247−2251.
(47) Kabalah-Amitai, L.; Mayzel, B.; Kauffmann, Y.; Fitch, A. N.; Bloch, L.; Gilbert, P. U. P. A.; Pokroy, B. Vaterite Crystals Contain Two Interdispersed Structures. *Science* **2013**, *340*, 454−457.
(48) Lindenberg, C.; Scholl, J.; Vicum, L.; Mazzotti, M.; Brozio, J. L-Glutamic Acid Precipitation: Agglomeration Effects. *Cryst. Growth Des.* **2008**, *8*, 224−237.
(49) Collier, A. P.; Hounslow, M. J. Growth and Aggregation Rates for Calcite and Calcium Oxdalate Monohydrate. *AIChE J.* **1999**, *45*, 2298−2305.
(50) Zauner, R.; Jones, A. Determination of Nucleation, Growth, Agglomeration, and Disruption Kinetics from Experimental Precipitation Data: the Calcium Oxalate System. *Chem. Eng. Sci.* **2000**, *55*, 4219−4232.
(51) Hostomsky, J.; Jones, A. Calcium Carbonate Crystallization, Agglomeration and Form During Continuous Precipitation from Solution. *J. Phys. D: Appl. Phys.* **1991**, *24*, 165−170.
(52) David, R.; Espitalier, F.; Cameirao, A.; Rouleau, L. Developments in the Understanding and Modeling of the Agglomeration of Suspended Crystals in Crystallization from Solutions. *KONA* **2003**, *21*, 40−53.

DOI: 10.1021/acs.cgd.8b00116
Cryst. Growth Des. 2018, 18, 4306−4319

Supplementary Information

Thomas C. Farmer,[†] Sina K. Schiebel,[†,‡] Bradley F. Chmelka,[†] and Michael F. Doherty[*,†]

[†] *University of California, Santa Barbara, California, U.S.A.*

[‡] *Technical University of Munich, Munich, Germany*

E-mail: mfd@ucsb.edu

S1: Summary of $CaCO_3$ chemistry

Precipitator dynamics were monitored continuously via pH and at discrete 30 minute intervals with powder X-Ray diffraction on the effluent solids. Steady-state was declared when both measurements ceased changing in time ($\pm 3\%$ for phase fractions and ± 0.01 for pH). The process dynamics can be monitored with pH because the reaction equilibrium is very pH sensitive. A complete set of linearly independent reactions that occur in the MSMPR crystallizer are summarized below:

$$CO_2 + OH^- \rightleftharpoons HCO_3^- \tag{S1}$$

$$HCO_3^- + OH^- \rightleftharpoons CO_3^{2-} + H_2O \tag{S2}$$

$$H_2O \rightleftharpoons H^+ + OH^- \tag{S3}$$

$$Ca^{2+} + CO_3^{2-} \rightleftharpoons CaCO_{3,(s,i)} \tag{S4}$$

where $CaCO_{3,(s,i)}$ indicates solid form i. As reaction S4 (the precipitation) proceeds, CO_3^{2-} is removed from solution. By Le Chatelier's principle, this tends to drive reactions S1 and S2 forward, decreasing the pH. The reaction chemistry is coupled to the nucleation and

growth rates through the supersaturation. Therefore, the pH will not "line out" until the precipitation process has reached a steady-state, making pH a simple and effective leading steady-state indicator for the $CaCO_3$ system. Once the dynamic start-up phase of the experiment is complete, X-Ray diffraction phase fitting gives identical phase fractions for subsequent measurements spaced several residence times apart.

The equilibrium concentrations of CO_2, HCO_3^-, and CO_3^{2-} change as the pH is changed in a fixed volume of water with a fixed amount of carbon (closed batch system). At "high pH" essentially all of the carbon is in the CO_3^{2-} form. For the experiments discussed in this paper, the lowest steady-state pH value was 10.1 and typical values varied between 10.4 and 10.6. Just one tenth of a millimolar of net back reaction from Equation S2 is necessary to move the pH from 7 to 10, so choosing CO_3^{2-} as a carbon source for our experiments (i.e., Na_2CO_3) ensures that the experiment will operate at "high" pH.

S2: Model details

This section provides some of the mathematical details that were omitted from the main text for brevity. The governing partial differential integral equation is not derived here because an excellent, detailed derivaiton already exists in the published literature.[1] The Equation is repeated here for the reader's convenience.

$$\frac{\partial n_i(x)}{\partial t} + G_i \frac{\partial n_i(x)}{\partial x} = -\frac{n_i(x)}{\tau} + \frac{\beta x^2}{2} \int_0^x \frac{n_i((x^3-\lambda^3)^{1/3}) n_i(\lambda)}{(x^3-\lambda^3)^{2/3}} d\lambda - \beta n_i(x) \int_0^\infty n_i(\lambda) d\lambda \quad \text{(S5)}$$

$$B_i = k_{i,b}\left(\frac{C}{K_{eq,i}^{1/2}} - 1\right)^{b_i} \int_0^\infty x^2 n_i(t,x) dx \qquad G_i = k_{i,g}\left(\frac{C}{K_{eq,i}^{1/2}} - 1\right)^{g_i} \quad \text{(S6)}$$

$$i = \alpha, \beta, ... \qquad n_i(t=0,x) = n_{i,seed} \qquad n_i(t,x=0) = \frac{B_i}{G_i} \quad \text{(S7)}$$

where $n_{i,seed}$ represents the size distribution of seeds added to the crystallizer as a pulse at $t = 0$. The agglomeration kernel used here implies that agglomeration events can only occur among particles in the same distribution (of the same solid form). Multipolymorph agglomerates are observed in the SEM images reported in the main text, but one expects that the physical essence and perhaps the important effects of agglomeration can be captured and understood by this description. This simplification is discussed in more detail in section S3. The second governing equation for the model is the solute balance ODE.

$$\frac{dC}{dt} = \frac{C_0 - C}{\tau} - \sum_{i=\alpha,\beta} \rho_i k_{i,g} k_{i,v} \left(\frac{C}{K_{eq,i}^{1/2}} - 1 \right)^{g_i} \int_0^\infty n_i x^2 dx \tag{S8}$$

$$C(t = 0) = C_0 \tag{S9}$$

where C_0 is the inlet concentration. The method of moments changes some distribution function, $f(t, x)$, into an infinite set of moments that are explicitly independent of the variable, x, but that collectively retain much of the information relating the original function to the eliminated variable (x). The method of moments can be used to eliminate the x dependence from some distribution function $f(t, x)$ where $x \in [0, \infty)$ as shown below

$$m_0(t) = \int_0^\infty f(t, x) dx \tag{S10}$$

$$m_1(t) = \int_0^\infty x \ f(t, x) dx \tag{S11}$$

$$m_2(t) = \int_0^\infty x^2 \ f(t, x) dx \tag{S12}$$

$$m_k(t) = \int_0^\infty x^k \ f(t, x) dx \tag{S13}$$

In the precipitator model, the method of moments was used to transform the partial differential integral equation (Equation S5) in t and x into an infinite set of ODEs in just t. When

this procedure is followed, the moments take on physical significance; the zeroth moment is the total crystal number density, the first is the total particle length density, the second is related to the total particle surface area density through a shape factor ($k_{i,v}$), and the 3rd is related to the total crystal volume density through a shape factor. The k^{th} moment transformation of each term in Equation S5 is given in Equations S14-S20. Note that both populations (n_α and n_β) are generally functions of t and x. In the interest of simplicity of presentation, the time functionality of the $n_i(t,x)$ and $m_i(t)$ is implicit throughout much of this Supplementary Information. The first term in Equation S5 (farthest to the left):

$$\int_0^\infty x^k \ \frac{\partial n_i}{\partial t} dx = \frac{\partial}{\partial t} \int_0^\infty x^k \ n_i dx = \frac{dm_{i,k}}{dt} \tag{S14}$$

The second term requires integration by parts. When $k = 0$,

$$G_i \int_0^\infty \frac{\partial n_i}{\partial x} dx = B_i \tag{S15}$$

and the $k \neq 0$ case becomes

$$\int_0^\infty G_i \ x^k \frac{\partial n_i}{\partial x} dx = G_i \left[x^k n_i(t,x) \Big|_0^\infty - k m_{i,k-1} \right] = -k G_i m_{i,k-1} \tag{S16}$$

The third term:

$$\int_0^\infty -x^k \frac{n_i(t,x)}{\tau} dx = -\frac{m_{i,k}}{\tau} \tag{S17}$$

For the fourth term, it is helpful to first swap the order of integration

$$\int_0^\infty \frac{\beta x^{2+k}}{2} \int_0^x \frac{n_i((x^3-\lambda^3)^{1/3}) n_i(\lambda)}{(x^3-\lambda^3)^{2/3}} d\lambda dx = \frac{\beta}{2} \int_0^\infty \int_\lambda^\infty x^{2+k} \frac{n_i((x^3-\lambda^3)^{1/3}) n_i(\lambda)}{(x^3-\lambda^3)^{2/3}} dx d\lambda \tag{S18}$$

Then, it is helpful to make the change of variables, $u^3 = (x^3 - \lambda^3)$. (See Ref. 2)[2]

$$\frac{\beta}{2} \int_0^\infty \int_\lambda^\infty x^{2+k} \frac{n_i((x^3-\lambda^3)^{1/3}) n_i(\lambda)}{(x^3-\lambda^3)^{2/3}} d\lambda dx = \frac{\beta}{2} \int_0^\infty n_i(\lambda) \int_0^\infty (u^3+\lambda^3)^{k/3} n_i(u) du d\lambda \tag{S19}$$

The fifth term simplifies to

$$-\int_0^\infty x^k \beta n_i(x) \int_0^\infty n_i(\lambda) d\lambda dx = -\beta m_k m_0 \tag{S20}$$

And since the i form nucleation expression can be rewritten in terms of the second moment of the i distribution,

$$B_i = k_{i,b}\left(\frac{C}{K_{eq,i}^{1/2}} - 1\right)^{b_i} m_{i,2} \tag{S21}$$

the infinite set of moment equations describing the populations (n_i) can be written succinctly as Equations S22 and S23 below. For $k = 0$:

$$\frac{dm_{i,0}}{dt} = -\frac{m_{i,0}}{\tau} + k_{i,b}\left(\frac{C}{K_{eq,i}^{1/2}} - 1\right)^{b_i} m_{i,2} - \frac{\beta}{2} m_{i,0}^2 \tag{S22}$$

when $k \neq 0$

$$\frac{dm_{i,k}}{dt} = -\frac{m_{i,k}}{\tau} + kG_i m_{i,k-1} + \frac{\beta}{2}\int_0^\infty n_i(\lambda) \int_0^\infty (u^3 + \lambda^3)^{k/3} n_i(u) du d\lambda - \beta m_{i,k} m_{i,0} \tag{S23}$$

The only piece of the solute balance ODE affected by the transformation is the last term (on the far right of Equation S8: $4\pi\rho_i k_{i,g}\left(\frac{C}{K_{eq,i}^{1/2}} - 1\right)^{g_i} \int_0^\infty n_i x^2 dx$). This term represents the moles of solute deposited from the solution into the solid distribution of polymorph i (n_i) per unit volume per unit time. Crystals grow from the surface, so the total solid crystal deposition rate is a product of the linear growth rate and the total amount of surface area that exists in the distribution. The integral term is necessary to determine how much crystal surface area exists in the distribution. In Equation S8, $k_{i,v}$ is the shape factor that relates the crystal length coordinate to its surface area and volume. After the method of moments transformation, the solute balance ODE simplifies to

$$\frac{dC}{dt} = \frac{C_0 - C}{\tau} - \sum_{i=\alpha,\beta} \rho_i k_{i,g} k_{i,v}\left(\frac{C}{K_{eq,i}^{1/2}} - 1\right)^{g_i} m_{i,2} \tag{S24}$$

S3: The agglomeration kernel

A constant agglomeration kernel is assumed throughout this analysis, but it was noted during both the model introduction and the experimental discussion that agglomeration kernels have been proposed that depend on crystal size (x) and/or supersaturation (S, or C/C_{sat}).[3–5] While analyzing the steady-state structure and relative dynamic stability features as functionals of the agglomeration kernel are outside the scope of this work, we do include several brief discussion points here.

First and foremost, the model presented here led to insights for designing solid-form selective precipitators, evidenced by the pure vaterite distributions obtained experimentally. In general, we prefer to model complex systems with the simplest possible description that consistently accounts for all of the important physicochemical effects. Furthermore, when one attempts to experimentally characterize model parameters, such as rate constants or agglomeration kernels, a simpler description often requires less experimental data to test and is therefore less prone to parameter estimation errors, making it more useful. If a simple model fails to re-create observed experiments, one can then move to a more complicated model.

The agglomeration kernel utilized here also implies that agglomeration only occurs among crystals of the same solid form. This assumption is unlikely to be exactly true for all sets of design choices and operation conditions, but this treatment is not expected to limit the utility of the design rules. Only polymorphically pure steady-states are possible in the absence of agglomeration (See our previous paper[6]). Therefore, in the limit of low agglomeration rates, the first agglomeration events must be among crystals of the same solid form, implying that the kernel used here must be exact in these regions of parameter space. Furthermore, one expects that the agglomeration kernel remains qualitatively correct near the mixed-polymorph/pure polymorph bifurcation surfaces (the lines separating regions of pure-form dynamic stability from regions of mixed-form dynamic stability in Figure 2) because the polymorphic distribution changes continuously across these transitions. Immediately across

a bifurcation surface within the mixed-polymorph stability region, the crystal distribution remains dominated by a single solid form, thus most agglomeration events must be between crystals of that dominant solid form. These bifurcation surfaces collapse to a single surface in the limit $A_i \to 0$, further implying that this description becomes more accurate in that limit. The model retains its utility even if some set of operating conditions generates appreciable fractions of both solid forms and thus enables non-zero inter-form agglomeration rates because this is not a region of parameter space in which one would prefer to operate. The model need not quantitatively predict the value of all of the states deep within the region of mixed-polymorph stability for the design rules produced from it to be useful. The primary utility of the analysis presented here is the determination of the location of the bifurcation surfaces in parameter space, and the agglomeration kernel is very accurate near these surfaces. These design rules guide process design towards or away from the bifurcation surface that separate the regions of parameter space that produce preferred and unpreferred solid form distributions. Therefore, the positions of the bifurcation surfaces are more important than the relative distribution of the forms deep within the mixed-polymorph region. If the specific size distribution and solid fraction deep within the mixed-polymorph region is pertinent for some application, then one might consider how the model predictions change if a more detailed agglomeration kernel is utilized.

S4: Discussion of the functional form of the Damköhler numbers

The Damköhler numbers are defined in Equations 16 and 18 in the main text and re-stated here in Equations S25 and S26.

$$Da_\alpha = 2\tau k_{\alpha,b}\left(\frac{C_0 - K_{eq,\beta}^{1/2}}{K_{eq,\alpha}^{1/2}}\right)^{b_\alpha}\sigma_\alpha^2 > 0 \qquad Da_\beta = 2\tau k_{\beta,b}\left(\frac{C_0 - K_{eq,\beta}^{1/2}}{K_{eq,\beta}^{1/2}}\right)^{b_\beta}\sigma_\beta^2 > 0 \qquad \text{(S25)}$$

where σ_i is the characteristic growth length for form i defined as

$$\sigma_\alpha = \tau k_{\alpha,g}\left(\frac{C_0 - K_{eq,\beta}^{1/2}}{K_{eq,\alpha}^{1/2}}\right)^{g_\alpha} \qquad \sigma_\beta = \tau k_{\beta,g}\left(\frac{C_0 - K_{eq,\beta}^{1/2}}{K_{eq,\beta}^{1/2}}\right)^{g_\beta} \tag{S26}$$

Conventionally, the dimensionless groups that arise from non-dimensionalizing a set of model equations are presented as ratios of characteristic times or rates. When this convention is followed, all dimensionless groups have an intuitive meaning that is easy to understand, and one can often intuit how the model solution might change when the group changes based on this intuition alone. The presentation of the Damköhler numbers in the text attempts to follow this convention, but some additional discussion is required to reconcile the convention with the τ^3 scaling of both Da_i.

The nucleation rate expression used here is a secondary rate expression that scales with the second moment of the crystal size distribution. Therefore, $k_{i,b}$ has units of number/ length^2/time, and a characteristic area scale is required to estimate a characteristic nucleation rate with units of number/time. Upon non-dimensionalization, one determines that the characteristic area that appears in the dimensionless group is σ_i^2. The quantity σ_i contains a product of the growth rate expression prefactor ($k_{i,g}$; units of length/time) and the residence time which combine to give a length dimension. This length is the characteristic growth length for form i during a time period of one residence time τ, therefore σ_i^2 is a characteristic crystal surface area. In the context of the convention discussed above, a reasonable way to qualitatively describe the Da_i is as a ratio of the characteristic process time to the characteristic nucleation time, where the characteristic nucleation rate varies as the characteristic growth length squared (σ_i^2). The Da_i are similar to conventional Damköhler numbers in the context of this intuitive description.

S5: Non-stoichiometric feed and non-dimensionalization

The experiments reported in this paper took place at relatively high pH conditions. Therefore, we have assumed that the reactant salts were fully dissociated and that all of the aqueous carbon was in the carbonate form (CO_3^{2-}). In this case, the only relevant aqueous species are Ca^{2+} and CO_3^{2-}, and the chemistry can be summarized as:

$$Ca^{2+} + CO_3^{2-} \rightleftharpoons CaCO_{3,(s,\alpha)} \qquad\qquad Ca^{2+} + CO_3^{2-} \rightleftharpoons CaCO_{3,(s,\beta)} \tag{S27}$$

Therefore, there are $C - R = 2$ independent mole balances. Once the growth and nucleation rate expressions are defined, the solute balances for component 1 (Ca^{2+}) and component 2 (CO_3^{2-}) can be written:

$$\frac{dC_1}{dt} = \frac{C_{1,0} - C_1}{\tau} - 4\pi \sum_{i=\alpha,\beta} \rho_i k_{i,g} \left((\frac{C_1 C_2}{K_{eq,i}})^{1/2} - 1 \right)^{g_i} \int_0^\infty n_i x^2 dx \tag{S28}$$

$$\frac{dC_2}{dt} = \frac{C_{2,0} - C_2}{\tau} - 4\pi \sum_{i=\alpha,\beta} \rho_i k_{i,g} \left((\frac{C_1 C_2}{K_{eq,i}})^{1/2} - 1 \right)^{g_i} \int_0^\infty n_i x^2 dx \tag{S29}$$

$$B_i = k_{i,b} \left((\frac{C_1 C_2}{K_{eq,i}})^{1/2} - 1 \right)^{b_i} m_{i,2} \qquad\qquad G_i = k_{i,g} \left((\frac{C_1 C_2}{K_{eq,i}})^{1/2} - 1 \right)^{g_i} \tag{S30}$$

The 1/2 power that appears in the growth and nucleation driving forces was justified in a previous publication.[7] Subtracting Equation S28 from Equation S29 (at steady-state) yields the mole balance.

$$C_2 = C_{2,0} + C_1 - C_{1,0} \tag{S31}$$

Only one of the solute balances (S28 and S29) is linearly independent of equation S31. Now define $\phi = C_{2,0} - C_{1,0}$ to eliminate C_2 from Equation S28 to give a single solute balance in terms of C_1, $C_{1,0}$ and ϕ.

$$\frac{dC_1}{dt} = \frac{C_{1,0} - C_1}{\tau} - 4\pi \sum_{i=\alpha,\beta} \rho_i k_{i,g} \left(\left(\frac{C_1(C_1+\phi)}{K_{eq,i}} \right)^{1/2} - 1 \right)^{g_i} \int_0^\infty n_i x^2 dx \tag{S32}$$

The model is only meaningful for systems in which the feed is supersaturated, so the lowest possible value of C_1 is the value that gives a saturated solution, given ϕ. If $K_{eq,\beta}$ is the solubility product equilibrium constant of the least soluble form (calcite), then the limiting value of C_1 can be defined as a function of ϕ as shown in Equation S33.

$$C_{1,min} = \frac{(\phi^2 + 4K_{eq,\beta})^{1/2} - \phi}{2} \tag{S33}$$

$C_{1,min}$ is essentially the concentration expected to exist in the reactor after an infinite residence time. Notice that in the limit $\phi \to 0$ (i.e., a stoichiometric feed), $C_{1,min} \to K_{eq,\beta}^{1/2}$ (the expected result). Now that the minimum value of C_1 is known, one can non-dimensionalize C_1.

$$y = \frac{C_1 - C_{1,min}}{(C_{1,0}(C_{1,0}+\phi))^{1/2} - C_{1,min}} \tag{S34}$$

$y \in [0,1]$ when $\phi = 0$. If $\phi > 0$ or < 0, the upper bound for y is lower or higher, respectively. The non-stoichiometric non-dimensionalization generates four new dimensionless groups within the solute balance ODE:

$$y_0 = \frac{C_{1,0} - C_{1,min}}{(C_{1,0}(C_{1,0}+\phi))^{1/2} - C_{1,min}} \tag{S35}$$

$$\Gamma = \frac{K_{eq,\beta}^{1/2}}{(C_{1,0}(C_{1,0}+\phi))^{1/2} - C_{1,min}} \tag{S36}$$

$$\gamma = \frac{K_{eq,\beta}^{1/2} - K_{eq,\alpha}^{1/2}}{(C_{1,0}(C_{1,0}+\phi))^{1/2} - C_{1,min}} \tag{S37}$$

$$Z = \frac{(\phi^2 + 4K_{eq,\beta})^{1/2}}{(C_{1,0}(C_{1,0}+\phi))^{1/2} - C_{1,min}} = \Gamma\frac{(\phi^2 + 4K_{eq,\beta})^{1/2}}{K_{eq,\beta}^{1/2}} \tag{S38}$$

$$\frac{dy}{d\xi} = y_0 - y - \omega_{\beta,2}\left[(y^2 + Zy + \Gamma^2)^{1/2} - \Gamma\right]^{g_\beta} - \omega_{\alpha,2}\left[(y^2 + Zy + \Gamma^2)^{1/2} - \Gamma + \gamma\right]^{g_\alpha} \tag{S39}$$

With these definitions, the dimensionless states of both the moment equations and the solute balance can be defined as shown below

$$\xi = \frac{t}{\tau} > 0 \qquad\qquad y = \frac{C_1 - C_{1,min}}{(C_{1,0}(C_{1,0}+\phi))^{1/2} - C_{1,min}} \tag{S40}$$

$$\sigma_\alpha = \tau k_{\alpha,g}\left(\frac{1}{\Gamma - \gamma}\right)^{g_\alpha} \qquad\qquad \sigma_\beta = \tau k_{\beta,g}\left(\frac{1}{\Gamma}\right)^{g_\beta} \tag{S41}$$

$$\omega_{\alpha,0} = 8\pi\sigma_\alpha^3 m_{\alpha,0}\frac{\rho_\alpha}{C_0 - K_{eq,\beta}^{1/2}} \qquad\qquad \omega_{\beta,0} = 8\pi\sigma_\beta^3 m_{\beta,0}\frac{\rho_\beta}{C_0 - K_{eq,\beta}^{1/2}} \tag{S42}$$

$$\omega_{\alpha,1} = 8\pi\sigma_\alpha^2 m_{\alpha,1}\frac{\rho_\alpha}{C_0 - K_{eq,\beta}^{1/2}} \qquad\qquad \omega_{\beta,1} = 8\pi\sigma_\beta^2 m_{\beta,1}\frac{\rho_\beta}{C_0 - K_{eq,\beta}^{1/2}} \tag{S43}$$

$$\omega_{\alpha,2} = 4\pi\sigma_\alpha m_{\alpha,2}\frac{\rho_\alpha}{C_0 - K_{eq,\beta}^{1/2}} \qquad\qquad \omega_{\beta,2} = 4\pi\sigma_\beta m_{\beta,2}\frac{\rho_\beta}{C_0 - K_{eq,\beta}^{1/2}} \tag{S44}$$

In the limit $\phi \to 0$ (i.e., a stoichiometric feed), the following simplifications occur. $y_0 \to 1$, $Z \to 2\Gamma$, and $C_{1,min} \to K_{eq,\beta}^{1/2}$. After these simplifications, Equation S39 becomes

$$\frac{dy}{d\xi} = 1 - y - \omega_{\beta,2}y^{g_\beta} - \omega_{\alpha,2}(y+\gamma)^{g_\alpha} \tag{S45}$$

Equation S45 is equivalent to Equation 25 in the main text of the article.

When $\phi \to 0$, the dimensionless state definitions become:

$$\xi = \frac{t}{\tau} > 0 \qquad\qquad y = \frac{C_1 - K_{eq,\beta}^{1/2}}{C_0 - K_{eq,\beta}^{1/2}} \tag{S46}$$

$$\sigma_\alpha = \tau k_{\alpha,g}\left(\frac{C_0 - K_{eq,\beta}^{1/2}}{K_{eq,\alpha}^{1/2}}\right)^{g_\alpha} \qquad \sigma_\beta = \tau k_{\beta,g}\left(\frac{C_0 - K_{eq,\beta}^{1/2}}{K_{eq,\beta}^{1/2}}\right)^{g_\beta} \tag{S47}$$

$$\omega_{\alpha,0} = 8\pi\sigma_\alpha^3 m_{\alpha,0}\frac{\rho_\alpha}{C_0 - K_{eq,\beta}^{1/2}} \qquad \omega_{\beta,0} = 8\pi\sigma_\beta^3 m_{\beta,0}\frac{\rho_\beta}{C_0 - K_{eq,\beta}^{1/2}} \tag{S48}$$

$$\omega_{\alpha,1} = 8\pi\sigma_\alpha^2 m_{\alpha,1}\frac{\rho_\alpha}{C_0 - K_{eq,\beta}^{1/2}} \qquad \omega_{\beta,1} = 8\pi\sigma_\beta^2 m_{\beta,1}\frac{\rho_\beta}{C_0 - K_{eq,\beta}^{1/2}} \tag{S49}$$

$$\omega_{\alpha,2} = 4\pi\sigma_\alpha m_{\alpha,2}\frac{\rho_\alpha}{C_0 - K_{eq,\beta}^{1/2}} \qquad \omega_{\beta,2} = 4\pi\sigma_\beta m_{\beta,2}\frac{\rho_\beta}{C_0 - K_{eq,\beta}^{1/2}} \tag{S50}$$

All of the experiments reported here were performed with a stoichiometric feed and at high enough pH such that Equation S27 is representative of the chemistry. In this case, C_1 becomes C, $y \in [0, 1]$ and Equation S45 is the only necessary solute balance ODE.

The quantity $K_{eq,\beta}$ appears in the definitions of σ_α and Da_α because the solute concentration is non-dimensionalized with respect to $K_{eq,\beta}$ (See Equation S46). The driving force for form i nucleation is

$$\left(\frac{C}{K_{eq,i}^{1/2}} - 1\right)^{b_i} \tag{S51}$$

From Equation S46, the dimensional concentration is equivalently given as

$$C = y\big(C_0 - K_{eq,\beta}^{1/2}\big) + K_{eq,\beta}^{1/2} \tag{S52}$$

Therefore, the driving force for form i nucleation can also be written as

$$\left(\frac{y\big(C_0 - K_{eq,\beta}^{1/2}\big) + K_{eq,\beta}^{1/2}}{K_{eq,i}^{1/2}} - 1\right)^{b_i} \tag{S53}$$

which can be re-written again as

$$\left(\frac{y\left(C_0 - K_{eq,\beta}^{1/2}\right)}{K_{eq,i}^{1/2}} + \frac{K_{eq,\beta}^{1/2}}{K_{eq,i}^{1/2}} - \frac{K_{eq,i}^{1/2}}{K_{eq,i}^{1/2}}\right)^{b_i} \tag{S54}$$

Or

$$\left(\frac{C_0 - K_{eq,\beta}^{1/2}}{K_{eq,i}^{1/2}}\right)^{b_i} \left(y + \frac{K_{eq,\beta}^{1/2} - K_{eq,i}^{1/2}}{C_0 - K_{eq,\beta}^{1/2}}\right)^{b_i} \tag{S55}$$

When $i = \beta$, this expression simplifies to

$$\left(\frac{C_0 - K_{eq,\beta}^{1/2}}{K_{eq,\beta}^{1/2}}\right)^{b_i} y^{b_i} \tag{S56}$$

When $i = \alpha$, it changes to

$$\left(\frac{C_0 - K_{eq,\beta}^{1/2}}{K_{eq,\alpha}^{1/2}}\right)^{b_i} \left(y + \frac{K_{eq,\beta}^{1/2} - K_{eq,\alpha}^{1/2}}{C_0 - K_{eq,\beta}^{1/2}}\right)^{b_i} = \left(\frac{C_0 - K_{eq,\beta}^{1/2}}{K_{eq,\alpha}^{1/2}}\right)^{b_i} (y + \gamma)^{b_i} \tag{S57}$$

The driving force for α form nucleation depends on $K_{eq,\beta}$ when written in terms of the dimensionless concentration, y. Therefore, $K_{eq,\beta}$ appears in the definition of Da_α. The same arguments apply to the driving force for α form growth. Therefore, the α form characteristic growth length, σ_α, also depends on $K_{eq,\beta}$ when written in terms of the dimensionless concentration, y.

S6: Crystal drying procedure

The data in Table S1 support the claim that polymorph transition does not occur during the drying procedure described in the experimental section. The table reports how the percent polymorph (by mass) of three different samples changed as a function of drying procedure. Each sample was measured without drying, after drying for 1 hour at 70 °C, and after drying for 72 hours at 70 °C. The phase fractions were the same for all drying procedures (within

experimental error). In all subsequent experiments, solids were dried for 24 hours at 70 °C before measuring the phase fractions with XRD. A similar procedure was followed in several published articles.[8,9]

Table S1: Each sample was collected from experiments performed at $T = 25°C$ with $\tau = 6$ minutes. Samples 1, 2 and 3 were performed with $C_0 = 0.0125$, 0.05, and 0.15 moles/liter, respectively. The samples were taken during startup dynamics to ensure that the initial distribution would contain both vaterite and calcite. The percent polymorph (mass) did not change when the drying procedure was varied.

Sample	preparation	% calcite	% vaterite	% aragonite
1	moist	73	27	0
	dried 1 hr	73	27	0
	dried 72 hr	73	27	0
2	moist	70	30	0
	dried 1 hr	70	30	<1
	dried 72 hr	70	30	<1
3	moist	64	36	0
	dried 1 hr	64	35	<1
	dried 72 hr	64	35	<1

S7: Reproducibility

We duplicated one set of experimental conditions to confirm that our experimental procedure was reproducible. The repeated experiment was performed with a residence time of $\tau = 12$ minutes, a temperature of $T = 25$ °C, and an inlet concentration of 0.0125 molar. As in all of the experiments, there is some noise ($\approx 3\%$) in the phase fitting results, but the average of the readings can be compared. The data in Table S2 illustrate that the experiment is reproducible within the error of the phase fitting. The average phase fraction measured at steady state in sample 1 and sample 2 was 95 and 94 wt. %, respectively. We therefore declare this experiment reproducible.

Table S2: Percent polymorph was characterized with powder XRD phase fitting at 30 minute intervals. The experiments described here were performed at $T = 25$°C, $\tau = 12$ minutes, and $C_0 = 0.0125$ molar. The table reports the maximum, minimum, and average polymorph % calculated from the powder XRD patterns taken after the process reached steady-state. The noise in the measurement is evident in the spread between the maximum and minimum values that were observed. The experimental observation was reproducible within the error of the measurement ($\approx \pm 3\%$).

Sample	max %	min %	mean %
1	95	93	94
2	96	93	95

S8: Additional NMR spectra and XRD patterns

Throughout this paper, the primary technique used to quantify phase fractions was Rietveld phase fitting of powder XRD patterns. This method is quick and accurate whenever the phase domains are large enough to reflect Xrays. Figures S1 and S2 were acquired on the steady-state effluent crystals from the experiments described in Figures 5a and 5b in the main text of this publication. Rietveld phase fitting of the pattern in Figure S1 and S2 indicate that the solids are 75 % and 93 % vaterite, respectively. Complementary ^{43}Ca

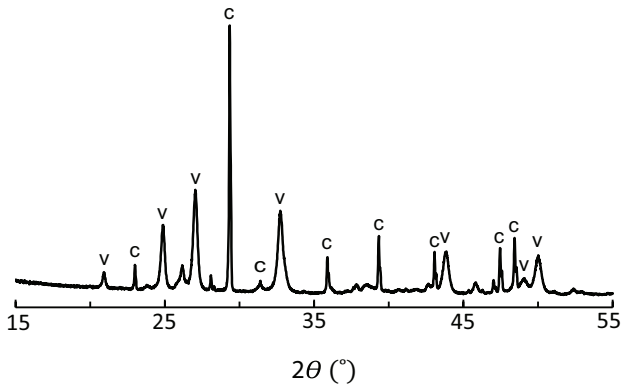

Figure S1: Powder X-ray diffraction pattern collected on solids removed from the steady-state precipitation experiment described in Figure 5a of the main text of this publication. The experiment was performed at $T = 25$ °C, $\tau = 6$ min, and C_0=0.0125 M. Rietveld phase fitting indicates that the solids are 75 % vaterite and 25 % calcite.

NMR spectra were acquired on two select samples to determine the local ^{43}Ca environments associated with the different $CaCO_3$ phases. ^{43}Ca is difficult to characterize with NMR due

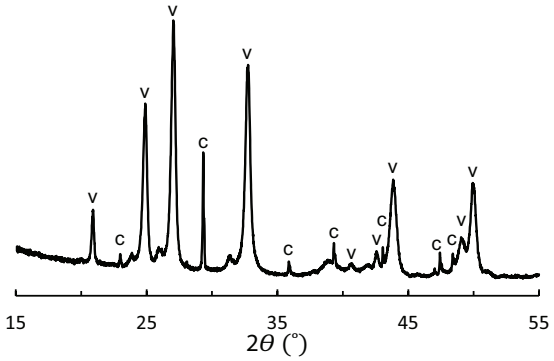

Figure S2: Powder X-ray diffraction pattern collected on solids removed from the steady-state precipitation experiment described in Figure 5b of the main text of this publication. The experiment was performed at T = 25 °C, τ= 9 min, and C_0=0.0125 M. Rietveld phase fitting indicates that the solids are 93 % vaterite and 7 % calcite.

to its low gyromagnetic ratio (-1.803 $\times$ 10^7 rad T^{-1} s^{-1}), low natural isotopic abundance ($\approx$ 0.135 %), and the general difficulties associated with quadrupolar nuclei (7/2 spin). These challenges were overcome with the high magnetic fields (19.6 T) possible at the U.S. National High Magnetic Field Laboratory in Tallahassee, Florida. The spectrum in Figure S3 was acquired on a solid sample known to contain aragonite, calcite, and vaterite. This sample was chosen to confirm that each solid form displays unique, resolvable chemical shifts under our experimental conditions. A second spectrum (Figure 8b) was acquired on a sample produced in our precipitator for which XRD indicated that the sample was predominantly vaterite (< 1% calcite). The single peak centered around 3 ppm in Figure 8b indicates that the only form present within the detection of the measurement is vaterite. This corroborates the powder XRD data, and the SEM images presented in the main text (Figure 8a, c, d). Therefore, vaterite is the only detectable solid form in the sample obtained at a residence time of 6 minutes, an inlet concentration of 0.15 molar, and a temperature of 25 °C.

The centers of the NMR peaks associated with calcite, vaterite, and aragonite are sensitive to the molar concentration of the aqueous $CaCl_2$ used to reference the spectrum, but the broad vaterite peak is found between the calcite and aragonite peaks for all reference

concentrations.[10]

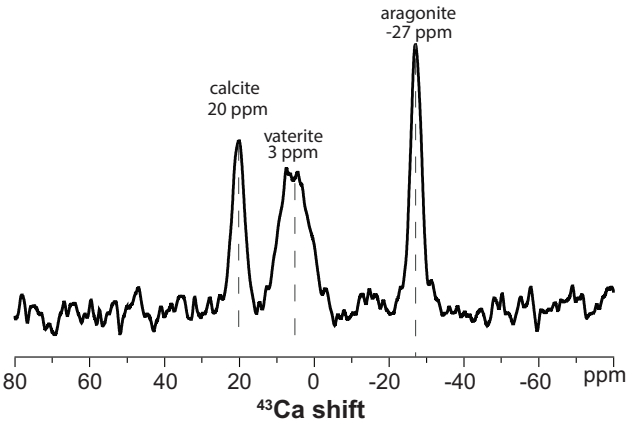

Figure S3: Solid-state, single pulse ^{43}Ca NMR spectrum acquired from a solid sample known to contain vaterite, aragonite, and calcite (from XRD phase fitting). The NMR spectrum was acquired at 19.6 T, 25 °C, and 5 kHz MAS with a 0.5 s delay time. The peaks at 20, 3 and -27 ppm can be assigned to calcite, vaterite, and aragonite, respectively. This measurement confirms that all three solid forms have resolvable chemical shifts at these conditions.

S9: Additional discussion of model analysis

When the stability transitions are projected onto the 2-dimensional Φ_α vs. Φ_β plane as in Figure 3 (main text of this article), the location of the mixed-polymorph/pure-polymorph bifurcation lines are strong functions of the Agglomeration numbers and weak functions of all of the other parameters. The two stability transition boundaries that mark the dynamic stability transition from a pure α or a pure β steady-state to a mixed-polymorph steady-state move away from the $\Phi_\alpha = \Phi_\beta$ line as the Agglomeration numbers increase from zero. In the main text of the article, A_α^{crit} was identified as the lowest value of A_α for which the mixed-polymorph steady-state is possible at a fixed value of the other 8 parameters such that $\Phi_\alpha > \Phi_\beta$. Our numerical results consistently show that this critical agglomeration number occurs when the steady-state solute concentration at the pure α steady-state is exactly equal to the steady-state concentration at the pure β steady-state in the limit of $A_\beta \to 0$. The mixed-polymorph steady-state also becomes linearly stable when $A_\alpha > A_\alpha^{crit}$.

A similar critical agglomeration number (A_β^{crit}) exists when $\Phi_\beta > \Phi_\alpha$. Qualitatively, this pure β/mixed-polymorph bifurcation surface similarly corresponds to all of the parameter combinations at which the solute concentration (y) is the same at both the pure β steady-state ($A_\beta \neq 0$) and the pure α steady-state when $A_\alpha = 0$ (i.e., $y_{\beta,A_\beta\neq 0} = f(Da_\beta, g_\beta, b_\beta, A_\beta) = y_{\alpha,A_\alpha=0} = g(Da_\alpha, g_\alpha, b_\alpha, \gamma)$). Analogously, the mixed-polymorph steady-state is linearly stable when $A_\beta > A_\beta^{crit}$.

Therefore, the position of each bifurcation surface projection in the Φ_α vs Φ_β plane that separates a region of pure polymorph dynamic stability from a region of mixed-polymorph dynamic stability depends on only one of the Agglomeration numbers. When $\Phi_\alpha > \Phi_\beta$, the important Agglomeration number for relative dynamic stability is A_α. Alternatively, when $\Phi_\alpha < \Phi_\beta$, the important Agglomeration number for relative dynamic stability is A_β. Each of the stability diagrams in this article were calculated with $A_\beta = A_\alpha$. The same information could have been presented with $A_i = 0$, $A_j \neq 0$, and twice as many figures. In other words, each Agglomeration number only affects the stability relationships for 1/2 of the stability diagram ($\Phi_{i=q} > \Phi_{i\neq q}$). Each stability diagram presented at fixed $A_\alpha = A_\beta$ is technically a projection of the four dimensional stability space defined by $[\Phi_\alpha, \Phi_\beta, A_\alpha, A_\beta]$ onto the two dimensional plane defined by $[\Phi_\alpha, \Phi_\beta, A_\alpha = A_\beta = A]$ (where A is some constant). Based on all of our calculations, we believe that no information is lost when the results are presented and discussed in terms of a three dimensional stability space defined by $[\Phi_\alpha, \Phi_\beta, A_\alpha = A_\beta]$. Therefore, we presented and discussed all stability diagrams as two dimensional slices/projections of the three dimensional stability space defined by $[\Phi_\alpha, \Phi_\beta, A_\alpha = A_\beta = A]$

Figures S4-S6 demonstrate that the projections of the bifurcation surfaces onto the Φ_α and Φ_β plane are relatively insensitive to physically reasonable changes in the remaining parameters (g_α, b_α, g_β, b_β, and γ). In each figure, all but one parameter that affects each bifurcation surface is held constant at the "base case" values defined in Figure 3b of the main text of this paper ($g_i = 1.5$, $b_i = 2.5$, $\gamma = -0.0042$, and $A_i = 0.1$). Then, the mixed-polymorph stability boundary is projected onto the Φ_α, Φ_β plane for several different

physically reasonable values of the last parameter. The figure then illustrates how changing that parameter affects the position of the mixed-polymorph stability boundary.

In Figure S4, the mixed polymorph stability boundary is shown for g_α and $g_\beta = 1$, 1.5, and 2. Variation in both g_α and g_β is presented on the same figure because each parameter only affects the boundary on one side of the $\Phi_\alpha = \Phi_\beta$ line. Increasing the growth exponent while holding all of the other parameters constant grows the mixed-polymorph stability region, but has very little effect on the overall shape of the boundary.

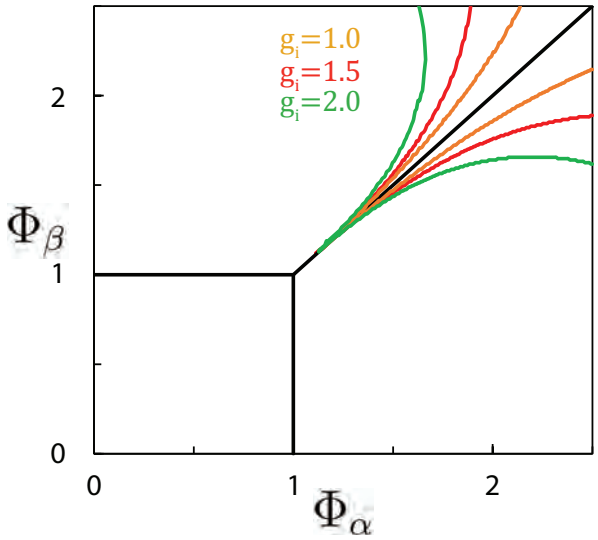

Figure S4: The outermost (green), middle (red), and inner (orange) curves are the mixed-polymorph/pure-polymorph stability transition boundaries when $g_i = 2$, 1.5, and 1, respectively. These curves were all calculated with the other 8 dimensionless model parameters fixed at the values associated with Figure 3b in the main text of the article ($b_\alpha = b_\beta = 2.5$, $\gamma = -0.0042$, and $A_\alpha = A_\beta = 0.1$)). The mixed-polymorph stability region is larger when the growth exponent is higher, but changing the growth exponent does not change the qualitative shape of the curve.

In Figure S5 the mixed-polymorph stability boundary is shown for b_α and $b_\beta = 1.5$, 2.5, and 3.5. Variation of the bifurcation surface projection's position in the Φ_α vs Φ_β plane with respect to both b_α and b_β is presented on the same figure because each b_i only affects the boundary on one side of the $\Phi_\alpha = \Phi_\beta$ line. The bifurcation surfaces are relatively insensitive to changes in b_i, but the total mixed-polymorph stability region does shrink as the b_i are increased.

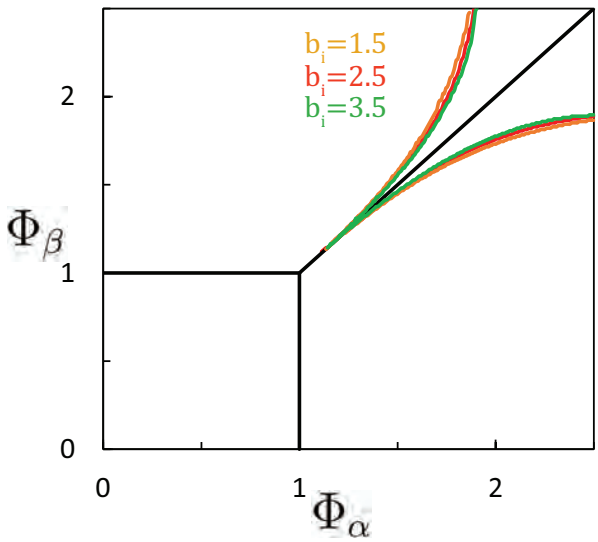

Figure S5: The outermost (orange), middle (red), and inner (green) curves are the mixed-polymorph/pure-polymorph stability transition boundaries when b_i = 1.5, 2.5, and 3.5, respectively. These curves were all calculated with the other 8 dimensionless model parameters fixed at the values associated with Figure 3b in the main text of the article ($g_\alpha = g_\beta = 1.5$, $\gamma = -0.0042$, and $A_\alpha = A_\beta = 0.1$)). The bifurcation surfaces are relatively insensitive to changes in b_i, but the total mixed-polymorph stability region does shrink as the b_i are increased.

In Figure S6 the mixed-polymorph stability boundary is shown for $\gamma = -0.0042$, -0.1, and -0.2. The solubility parameter (γ) exhibits no effect on the mixed-polymorph stability bifurcation surface above the $\Phi_\alpha = \Phi_\beta$ line, but it has a substantial effect on the surface below this line. γ quantifies the difference in solubility between the two forms relative to the inlet supersaturation of the most stable form. When it is close to zero (such as in the experiments reported here in which $\gamma \approx -0.0042$), the mixed polymorph bifurcation surfaces are almost symmetric around the $\Phi_\alpha = \Phi_\beta$ line. As γ approaches -1, the mixed polymorph-stability region grows below the $\Phi_\alpha = \Phi_\beta$ line, introducing considerable asymmetry.

S10: Vaterite stability data

Table S3 shows how the solid form of three different samples changed during storage. Each data point was determined by phase fitting of a powder X-Ray diffraction pattern. Samples

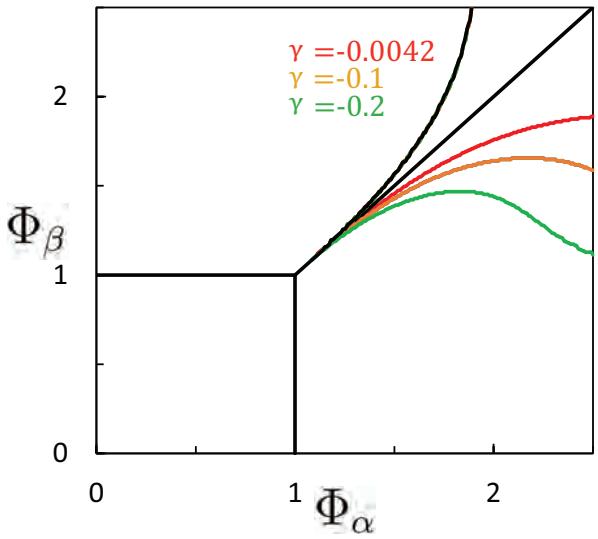

Figure S6: The outermost (green), middle (orange), and inner (red) curves are the mixed-polymorph/pure-polymorph stability transition boundaries when $\gamma = -0.2$, -0.1, and -0.0042, respectively. These curves were all calculated with the other 8 dimensionless model parameters fixed at the values associated with Figure 3b in the main text of the article ($g_\alpha = g_\beta = 1.5$, $b_\alpha = b_\beta = 2.5$, and $A_\alpha = A_\beta = 0.1$)). The position of the mixed-polymorph/pure polymorph stability transition surface projection onto the Φ_α vs Φ_β plane above the $\Phi_\alpha = \Phi_\beta$ line is not a function of γ. This is intuitively consistent because γ only affects the metastable form driving forces in the model. The position of the mixed-polymorph/pure polymorph stability transition surface projection onto the Φ_α vs Φ_β plane below the $\Phi_\alpha = \Phi_\beta$ line shows a relatively strong dependence on γ.

were filtered and dried as previously discussed. Crystals were then stored in a sealed vial for the time listed in the table. Dry vaterite prepared in this way is stable for at least 450 days.

Table S3: Three separate samples were monitored that initially contained >98% vaterite (based on X-Ray diffraction phase fitting). Changes in polymorph % that have been observed thus far are smaller than the error of the phase fitting procedure. Dry vaterite can be stable for at least 450 days without any additional additives or treatments.

Sample #	# of days	% calcite	% vaterite
1	0	1.1	98.9
	21	1.7	98.3
	31	1.1	98.9
2	0	0.5	99.5
	8	0.6	99.4
3	0	0.5	99.5
	≈450	2	98.0

S11: Estimating the nucleation rate expression pre-factor

In our earlier paper, we made comparisons to experimental results reported in two papers by Lai et al.[8,11] These papers reported secondary nucleation kinetics of the form:

$$B_i = k_{i,b,M_T^{2/3}} \left(\frac{C}{C_{sat,i}} - 1 \right)^{b_i} M_T^{2/3} = k_{i,b,M_T^{2/3}} \left(\frac{C}{C_{sat,i}} - 1 \right)^{b_i} (\rho_i m_{i,3})^{2/3} \tag{S58}$$

where B_i has units of number/length^3/time, M_T is the magma density in units of mass of solids per suspension volume, and ρ_i is the mass density of solute with units of mass of solids per solid volume. The analysis in this paper and in our previous paper[6] assumed that the

nucleation rate scaled with the second moment of the distribution, $m_{i,2}$.[1]

$$B_i = k_{i,b,m_2}\left(\frac{C}{C_{sat,i}} - 1\right)^{b_i} m_{i,2} \tag{S59}$$

For comparisons of our theory to the available experiments, we assumed that $m_2 \approx m_3^{2/3}$ such that the correct nucleation rate expression pre-factor adjustment was just $\rho_i^{2/3}$. In other words, we assumed that the nucleation rates predicted by our model would be approximately the same as the rates predicted by the rate model in Lai et al. once we redefined the nucleation rate pre-factor for our model (k_{i,b,m_2}) as the following function of the nucleation rate pre-factor in Lai et al.[8]

$$k_{i,b,m_2} = k_{i,b,M_T^{2/3}}\rho_i^{2/3} \tag{S60}$$

Since the units of the magma density used to regress $k_{i,b,M_T^{2/3}}$ were not specifically stated in Lai et al., we selected the units that gave the best agreement between calculated (using Equation S59) and experimental steady-state solution concentration (kg/L). This led to all of our assumed nucleation rate pre-factors (k_{i,b,m_2}) being $1.54^{2/3}$ times as large as the pre-factors reported in Lai et al. ($k_{i,b,M_T^{2/3}}$).[8]

In this section, we offer another, higher fidelity conversion that does not require the assumption $m_2 \approx m_3^{2/3}$. The simpler conversion (Equation S60) was used in Figure 9 in the main text of this manuscript for consistency, but both Figure 2 from our 2016 paper and Figure 9 from this paper have also been re-constructed under the higher fidelity conversion presented next. These figures are included at the end of Section S11, and they illustrate that both conversion approaches lead to solid form predictions that are consistent with the reported experimental data.

[1]We prefer Expression S59 because it allows the moment transformation to close 1 order lower ($k = 2$ instead of $k = 3$), and we expected that both expressions should exhibit similar predictive utility.

Higher fidelity transformation

In this section, we describe a higher fidelity nucleation rate expression conversion approach (relative to Equation S60) that is based on a more realistic description of the relationship between k_{i,b,m_2} and $k_{i,b,M_T^{2/3}}$. Therefore, it should better reproduce the reported experimental data and enable more effective generalizations to other experimental conditions.

MSMPR crystallizers dominated by nucleation and growth (with negligible agglomeration) exhibit the following steady-state crystal size distribution

$$n_i(x) = n_i(0)e^{-x/(G_i\tau)} \tag{S61}$$

Therefore, the steady-state moments are

$$m_{i,2} = 2n_i(0)(G_i\tau)^3 \tag{S62}$$

$$m_{i,3} = 6n_i(0)(G_i\tau)^4 \tag{S63}$$

$$\tag{S64}$$

and $M_T^{2/3}$ is

$$M_T^{2/3} = \left(6\rho_i n_i(0)(G_i\tau)^4\right)^{2/3} \tag{S65}$$

G_i is monotonically increasing in the steady-state supersaturation, and the steady-state supersaturation monotonically decreases with increases in τ. Therefore, for a specific crystal system at a specific feed concentration and temperature, $G_i\tau$ should be relatively constant. One can estimate a constant correction factor that converts from a nucleation rate proportional to $M_T^{2/3}$ to a rate proportional to m_2 by setting the two nucleation rate expressions

equal to each other and solving for the ratio $k_{i,b,m_2}/k_{i,b,M_T^{2/3}}$.[2]

$$k_{i,b,M_T^{2/3}}\left(\frac{C}{C_{sat,i}}-1\right)^{b_i}\left(6\rho_i n_i(0)(G_i\tau)^4\right)^{2/3} = k_{i,b,m_2}\left(\frac{C}{C_{sat,i}}-1\right)^{b_i} 2n_i(0)(G_i\tau)^3 \tag{S66}$$

$$k_{i,b,m_2}/k_{i,b,M_T^{2/3}} = \left(6\rho_i n_i(0)(G_i\tau)^4\right)^{2/3}/\left(2n_i(0)(G_i\tau)^3\right) \tag{S67}$$

$$k_{i,b,m_2}/k_{i,b,M_T^{2/3}} = \left(\frac{9\rho_i^2}{2n_i(0)G_i\tau}\right)^{1/3} \tag{S68}$$

The quantity $n_i(0)$ is estimated from the nucleation and growth rate expressions and the steady-state concentrations reported in Lai et al.

$$n_i(0) = B_i/G_i = k_{i,b,M_T^{2/3}}(C/C_{sat,i}-1)^{b_i}M_T^{2/3}/G_i \tag{S69}$$

$$n_i(0) = B_i/G_i = \ k_{i,b,M_T^{2/3}}(C/C_{sat,i}-1)^{b_i}\rho_i^{2/3}\left(6n_i(0)(G_i\tau)^4\right)^{2/3}/G_i \tag{S70}$$

$$[n_i(0)]^{1/3} = k_{i,b,M_T^{2/3}}(C/C_{sat,i}-1)^{b_i}\rho_i^{2/3}\left(6(G_i\tau)^4\right)^{2/3}/G_i \tag{S71}$$

$$n_i(0) = \frac{(k_{i,b,M_T^{2/3}}(C/C_{sat,i}-1)^{b_i})^3\left(\rho_i 6(G_i\tau)^4\right)^2}{G_i^3} \tag{S72}$$

Expression S68 and S72 combine to give

$$k_{i,b,m_2}/k_{i,b,M_T^{2/3}} = \left(\frac{9\rho_i^2}{2[n_i(0)]G_i\tau}\right)^{1/3}\frac{G_i}{(k_{i,b,M_T^{2/3}}(C/C_{sat,i}-1)^{b_i})\left(\rho_i 6(G_i\tau)^4\right)^{2/3}} \tag{S73}$$

Collecting like terms

$$k_{i,b,m_2}/k_{i,b,M_T^{2/3}} = \frac{1}{2k_{i,b,M_T^{2/3}}G_i^2(C/C_{sat,i}-1)^{b_i}\tau^3} \tag{S74}$$

The steady-state concentrations and growth kinetics are reported for each of the 6 experiments in Lai et al.[8] This information can be combined with Equation S74 to determine a higher fidelity estimate for the conversion factor from one nucleation rate expression to the other. In fact, this transformation guarantees that the nucleation rates will be exactly the

[2] $k_{i,b,m_2}/k_{i,b,M_T^{2/3}}$ is also called the "adjustment factor" throughout this section.

same for both expressions exactly at the operating point in question. Unfortunately, we can only do this adjustment for a solid-form that is observed at steady-state (and presumably maintains a crystal size distribution defined by Equations S61 and S69). Still, one expects that the correct factor for some set of conditions should be approximately correct for some similar set of conditions (i.e., where that solid form is not observed), so calculating an average factor for the available data and extrapolating to other conditions seems reasonable.

These higher fidelity conversion factors have been calculated and reported in Table S4 for each of the 6 experiments in Lai et al. (where "adjustment factor" refers to $k_{i,b,m_2}/k_{i,b,M_T^{2/3}}$). The first four apply to the α polymorph of L-glutamic acid, and the last two apply to the β polymorph of L-glutamic acid. The average "adjustment factor" for the four pure α form steady-states is 11.32, and the average "adjustment factor" for the two pure β form steady-states is 0.80. The α "adjustment factor" is larger and the β factor is smaller than our previous estimates, so all data points move down and to the right in Figure 2 of our previous paper[6] and in Figure 9 in this manuscript. The theory correctly predicts the solid form reported in the experiments when the nucleation rate pre-factor is estimated with either method. Furthermore, it also predicts the steady-state solution concentrations reported in

Table S4: Higher fidelity adjustment factors (i.e., $k_{i,b,m_2}/k_{i,b,M_T^{2/3}}$) calculated from Equation S74 for the 6 experiments reported in Lai et al.[8] Figures S7 and S8 were generated by assuming the average adjustment factor of Experiments 1-4 (11.32) for k_{α,b,m_2} and the average adjustment factor of Experiments 5 and 6 (0.80) for k_{β,b,m_2}.

Exp #	"adjustment factor"	form
1	9.38	α
2	10.90	α
3	12.09	α
4	13.05	α
5	0.36	β
6	1.24	β

Lai et al. with high accuracy.

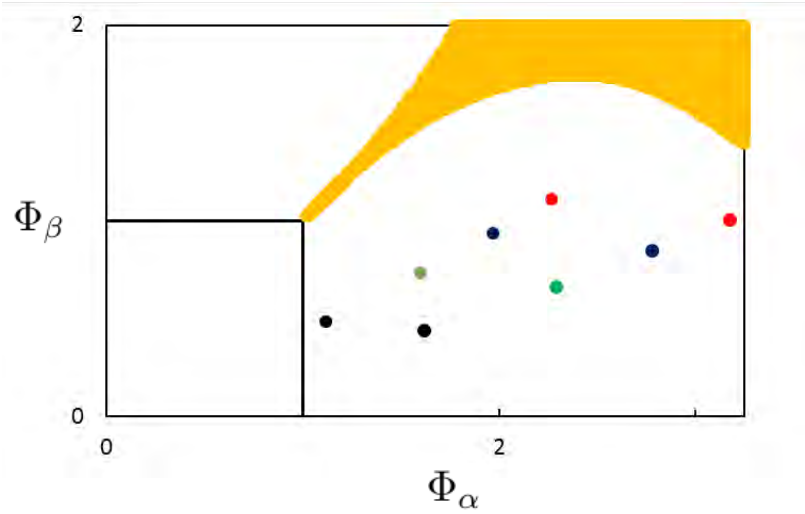

Figure S7: An illustration of how Figure 9 from the main text of this paper changes if one changes the nucleation rate conversion approach as described in this section (Equations S60 and S74). The points that are lower and to the right are for the higher fidelity conversion described in this section (Equation S74). The points move down and to the right because the higher fidelity conversion factor was lower for the β form ($0.80 < 1.54^{2/3}$) and higher for the α form ($11.32 > 1.54^{2/3}$). The black, green, blue, and red points correspond to experiments 1, 2 3, and 4, respectively.[8]

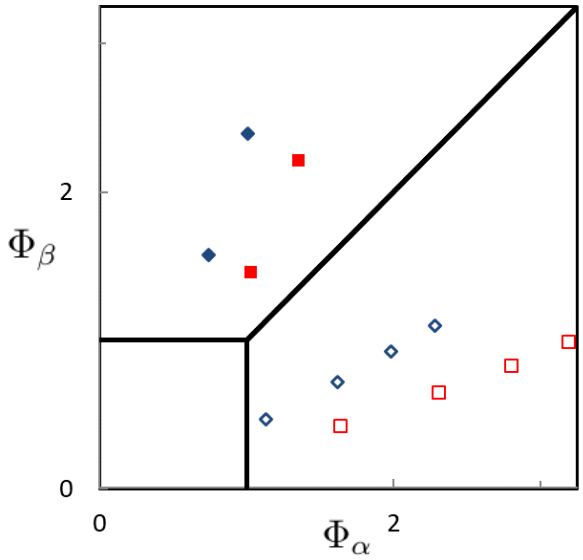

Figure S8: An illustration of how Figure 2 from the our 2016 paper[6] changes if one changes the nucleation rate conversion approach as described in this section. Here, the blue points represent the conversion by Equation S60 and the red points correspond to the conversion by Equation S74. The points that are lower and to the right are for the higher fidelity conversion (Equation S74) described in this section. The points move down and to the right because the higher fidelity conversion factor was lower for the β form ($0.80 < 1.54^{2/3}$) and higher for the α form ($11.32 > 1.54^{2/3}$).

References

(1) Ramkrishna, D. *Population Blances: Theory and Application to Particulate Systems in Engineering*; Academic Press, 2000.

(2) Marchisio, D. L.; Pikturna, J. T.; Fox, R. O.; Vigil, R. D.; Barresi, A. A. Quadature Method of Moments for Population-Balance Equations. *AIChE J.* **2004**, *49*, 1266–1276.

(3) Lindenberg, C.; Scholl, J.; Vicum, L.; Mazzotti, M.; Brozio, J. L-Glutamic Acid Precipitation: Agglomeration Effects. *Cryst. Growth Des.* **2008**, *8*, 224–237.

(4) Collier, A. P.; Hounslow, M. J. Growth and Aggregation Rates for Calcite and Calcium Oxdalate Monohydrate. *AIChE J.* **1999**, *45*, 2298–2305.

(5) Mullin, J. W. *Crystallization*; Oxford: Butterworth-Heinemann, 1993; Chapter 8.

(6) Farmer, T. C.; Carpenter, C. L.; Doherty, M. F. Polymorph Selection by Continuous Crystallization. *AIChE J.* **2016**, *62*, 3505–3514.

(7) Dandekar, P.; Doherty, M. F. A mechanstic growth model for inorganic crystals: Growth mechanism. *AIChE J.* **2014**, *60*, 3720–3731.

(8) Lai, T.; Ferguson, S.; Palmer, L.; Trout, B. L.; Myerson, A. S. Continuous Crystallization and Polymorph Dynamics in the L-Glutamic Acid System. *Org. Process Res. Dev.* **2014**, *18*, 1382–1390.

(9) Kralj, D.; Brecevic, L.; Nielson, A. E. Vaterite Growth and Dissolution in Aqueous Solution I. Kinetics of Crystal Growth. *J. Cryst. Growth* **1990**, *104*, 793–800.

(10) Bryce, D. L.; Bultz, E. B.; Aebi, D. Calcium-43 Chemical Shift Tensors as Probes of Calcium Binding Environments. Insights into the Structure of the Vaterite $CaCO_3$ Polymorph by ^{43}Ca Solid-State NMR Spectroscopy. *J. Am. Chem. Soc.* **2008**, *130*, 9282–9292.

(11) Lai, T. C.; Cornevin, J.; Ferguson, S.; Li, N.; Trout, B. L.; Myerson, A. S. Control of Polymorphism in Continuous Crystallization via Mixed Suspension Mixed Product Removal Systems Cascade Design. *Cryst. Growth Des.* **2015**, *15.7*, 3374–3382.